Design of Superconducting Transmission Line Integrated Surface-Electrode Ion-Traps

by

David Thomas Meyer

B.S., University of Washington (2009)

Submitted to the Department of Electrical Engineering and Computer Science
in partial fulfillment of the requirements for the degree of

Master of Science in Electrical Engineering and Computer Science

at the

MASSACHUSETTS INSTITUTE OF TECHNOLOGY

June 2011

Author ....
Department of Electrical Engineering and Computer Science
May 20, 2011

Certified by. .....
Karl K. Berggren
Professor
Thesis Supervisor

Accepted by ... .
Leslie A. Kolodziejski
Chair, Department Committee on Graduate Theses

Design of Superconducting Transmission Line Integrated Surface-Electrode Ion-Traps

by

David Thomas Meyer

Submitted to the Department of Electrical Engineering and Computer Science
on May 20, 2011, in partial fulfillment of the
requirements for the degree of
Master of Science in Electrical Engineering and Computer Science

Abstract

We fabricated superconducting surface electrode ion traps with integrated microwave coplanar waveguides using direct-write optical lithography and a niobium on sapphire process. We then tested these traps in a closed cycle cryostat and used 28 mW of microwave power to excite rotational transitions of trapped strontium chloride molecular ions. We expected that driving these rotational transitions would heat a co-trapped strontium atomic ion cloud. However, we did not see this heating and we must conduct further experiments.

Thesis Supervisor: Karl K. Berggren
Title: Professor

Acknowledgments

I have loved working in the Quantum Nanostructures and Nanofabrication group for the past two years. I am grateful to my colleagues for their support and friendship. It has also been a great pleasure to work so closely with the Quanta Group.

I would first like to thank my advisor Karl Berggren for giving me the opportunity to work on this interdisciplinary project. I would also like to thank Issac Chuang for his guidance on my research. Both Karl and Ike have truly inspired me during my time at MIT with their work ethic and integrity.

Next I would like to thank, Adam McCaughan who has worked with me to build my understanding of the fabrication and testing of our devices. I would also like to thank Anders Mortensen for being a guide into the realm of ion traps and the dark world of physics, and I wish him luck in his future career.

Francesco Marsili, Faraz Najafi, Hasan Korre and Francesco Bellei have helped increase my understanding of superconducting devices and low-temperature testing. Similarly, I have learned much from Peter Herskind, Tony Kim and Paul Antohi about physics, ion traps and optics. I would also like to thank Jim Daley and Shannon Wang for their technical help in building my devices and teaching me how to use the necessary tools.

I would like to thank my family for their unending curiosity in what I am doing and for providing me with the love and support I needed. I would especially like to thank my wife Stephanie for putting up with me staying late at work, for her deft use of an editing pen and for caring so much for me.

This project has been funded by a generous grant from DARPA and my stipend has come from the Interdisciplinary Quantum Information Science and Engineering fellowship at MIT.

Contents

List of Figures

List of Tables

Chapter 1

Introduction

A quantum computer requires the ability to store and process quantum information in a fast and reliable way. Trapped ions, by their nature, only weakly interact with their environment. This makes trapped ions ideal for storing quantum information but makes computation more difficult. Superconducting quantum systems on the other hand, make ideal quantum processors because of their strong interactions. Our group is trying to harness the inherent advantages of each of these systems by bridging the gap between the superconducting qubits and trapped ions in order to implement a quantum computer.

1.1 Quantum Computation

Quantum computers have the potential to solve problems in computer science and physics much faster than any classical computer. If a quantum computer could be built, it could solve the computer science problem of how to factor large integers[20], which would mean much of internet security could be broken. Another less well known algorithm could aid the physics community by solving a large system of linear equations faster than any classical computer[9].

There are two timescales in any quantum computer, the time it takes to manipulate information stored in the system and the time it takes for information to be corrupted or lost, which in a quantum system is known as decoherence. Supercon-

ducting qubits can be quickly manipulated in tens of nanoseconds, but decohere on the scale of microseconds which is too short to store information[3, 6, 7, 22]. On the other hand, the decoherence time of trapped ions can be as long as a second but it takes almost a millisecond to perform operations[16, 17].

These two systems have natural advantages that lend themselves towards creating two essential components of a quantum computer. Our group has proposed an experiment to integrate a trapped ion quantum system with a microwave system similar to the microwave components used in superconducting qubit research.

1.2 Bridging the Gap

Our group is seeking to utilize a long lived trapped ion state to create a quantum storage system. Because of this, our group initially turned to hyperfine transitions as these are the longest lived trapped atomic ion states. Hyperfine transitions require large electric fields to quickly drive an atom from one level to another. It would be almost impossible to achieve these fields using the microwave techniques from superconducting qubit research. One alternative to using hyperfine transitions was to use trapped molecular ions. Trapped molecular ions have rotational states with similar lifetimes to hyperfine transitions, but these states can be driven with smaller electric fields.

Some of the initial work has already been done to integrate superconducting materials like niobium or niobium-nitride[23] with surface electrode ion traps capable of trapping molecular ions. Additionally the microwave transmission lines used in superconducting qubit research can be integrated into surface electrode ion traps with minimal changes to their geometry.

Other groups have proposed experiments with the same future goal as our group; integrating an ion system with superconducting qubits to create a quantum computer[1]. However, these experiments propose using neutral molecules, which cannot be trapped as strongly as molecular ions, to store quantum information. Trapping neutral molecules requires more complex optics than trapping molecular ions. Since our

group uses molecular ions and less complex optics, theoretically we will then be able to integrate our systems into a dilution refrigerator more easily than groups working trapped neutral molecules. Dilution refrigerators are necessary to perform superconducting qubit research and therefore are a necessary part of our proposed quantum computer.

Our group hopes to build a scalable quantum computation architecture by integrating superconducting qubits with trapped molecular ions. Ideally, the rotational transitions of molecular ions will serve as a quantum memory system while superconducting qubits will serve as the quantum processor. In order to prove that we can control the rotational levels of a polar molecular ion in this way, we designed an experiment to sympathetically heat a strontium ion cloud by driving the rotational transitions of co-trapped strontium chloride molecular ions.

In our experiment we trapped a mixed species ion cloud of strontium atomic ions and strontium chloride molecular ions in a superconducting-transmission-line-integrated surface-electrode ion trap. Then, using doppler cooling, we lowered the temperature of the strontium ions, which in turn sympathetically cooled the strontium chloride. We then input high-power microwave signals to the integrated transmission line, which generated a large microwave field to drive rotational transitions in the strontium chloride ions. The energy from driving these rotational transitions can be mapped onto the kinetic energy of the ion cloud through collisional interactions[2]. Although we have not seen the resultant heating as of this writing, it should be observable using laser-induced fluorescence of the strontium atomic ions.

1.3 Thesis Overview

In Chapter 2 I discuss the basics of ion traps using the linear quadrupole ion trap. The symmetries of linear quadrupole ion traps make the analysis of these traps less complicated. I use these linear quadrupole traps as an example to formulate the equations of motion for ions in an ion trap and introduce the pseudopotential. The pseudopotential and the stability parameters of ion traps make it possible to predict

the results of mass spectroscopy scans which helps verify that we have loaded both the strontium (Sr^+) and strontium chloride ($SrCl^+$) required to perform our experiment. In this chapter I also outline laser cooling by the Doppler effect and the imaging process that is used to measure the expected heating of the Sr^+ ions.

In Chapter 3 I use the tools from Chapter 2 to analyze the surface electrode ion traps used in our experiment. Our experiment uses superconducting surface electrode ion traps integrated with coplanar waveguide transmission lines. These traps use square shaped electrodes on a dielectric substrate instead of the 3-D structures used in the linear Paul-traps. I also calculate the trapping parameters for our traps and show that both the Sr^+ and $SrCl^+$ are stable. If the Sr^+ and $SrCl^+$ are stable then we can conduct the experiment to look for heating caused by driving the rotational transitions in $SrCl^+$.

In Chapter 4 I calculate the expected voltage on the center electrode of coplanar waveguide (CPW) transmission lines and I use this voltage to calculate the microwave electric field at the $SrCl^+$ ions. According to our predictions this electric field will induce rotational transitions and heat the Sr^+ ion cloud[2].

In Chapter 5 I outline the necessary steps in the fabrication process and detail the components of the experimental apparatus. Our superconducting-transmission-line-integrated ion traps are fabricated with a niobium on sapphire process and then tested in a closed-cycle cryostat. In this chapter I also examine the design changes to the cryostat setup which were made to ensure superconductivity of the traps. I also discuss the optical and electrical networks used to generate, trap, image and manipulate the ions in order to show heating of the ion cloud as a result of driving rotational transitions in $SrCl^+$.

In Chapter 6 I discuss our preliminary experimental results and the major design changes to the ion traps that we tested. I also present the tests that we used to verify that the changes we made to the cryostat actually achieved superconductivity in our ion traps. The preliminary results of our heating experiment have not yet shown the expected temperature increase of the ion cloud, therefore I also present the future plans for this experiment.

Chapter 2

Electric Quadrupole Traps

In order to demonstrate that it is possible to drive rotational transitions in $SrCl^+$ we have to build an ion trap. We designed our ion traps using the base knowledge provided by analyzing linear Paul-traps. We used this as our starting point because the symmetries of linear Paul-traps simplify the equations of motion and stability for ions in the trap. In our experiment, working ion traps allow us to verify the ion species that are present in our trap through mass spectroscopy. These traps also allow us to laser cool the ions, and image them with a fluorescence signal that can detect if we have heated the Sr^+ ions. In future experiments, an ideally designed ion trap will produce ion crystals which are more sensitive and thus more versatile.

2.1 Linear Radio Frequency Traps

Before we can perform mass spectroscopy or use lasers to cool and image the ions we must understand how the ions behave in the trap. Linear radio-frequency (RF) ion traps are the precursors to the ion traps used in our experiment and can be analyzed faster because these traps have symmetries not present in our surface-electrode traps. These symmetries simplify the equations of motion for the trapped ions which are governed by the Mathieu equation. In Chapter 3, I apply the knowledge from this section to the specific surface-electrode traps we used in our experiment.

Earnshaw's theorem says that it is not possible to trap ions with static electric

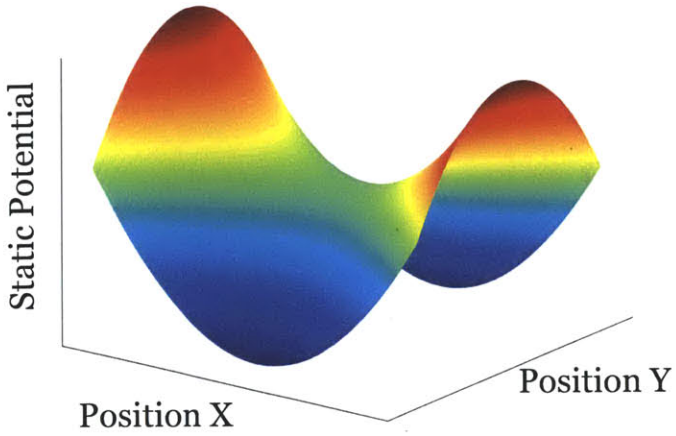

Figure 2-1: A saddle point in two dimensions. The color map corresponds to the plot height as well, red being high energy and blue being low energy. Physical systems work to minimize the potential energy so there is no stable point in this plot.

fields. However, it is possible to trap ions with oscillatory fields, as Wolfgang Paul demonstrated when he built the first successful ion trap using a radio frequency (RF) drive. The principle of the RF ion trap is to place an ion at a saddle point in a potential, like the one shown in Figure 2-1, and then rotate the saddle so that the ion cannot escape. These saddle points are quadrupole potentials that can be generated with four 3-D hyperbolic electrodes, two of which are at a high potential relative to the others.

The construction of 3-D hyperbolic electrodes is complicated but it is possible to generate an approximate quadrupole field using four cylindrical rods like those shown in Figure 2-2. This geometry is referred to as a linear quadrupole trap, or linear Paul-trap named after Wolfgang Paul for his pioneering research on RF traps. The quadrupole potential forms between the RF electrodes and the DC electrodes. When the RF signal is positive the ion drifts towards the DC electrodes, whereas when the RF electrodes are negative the ion moves towards the RF electrodes.

The frequency of the RF drive is small enough that the electro-quasistatic approximation is valid which makes it possible to write the potential of the linear trap

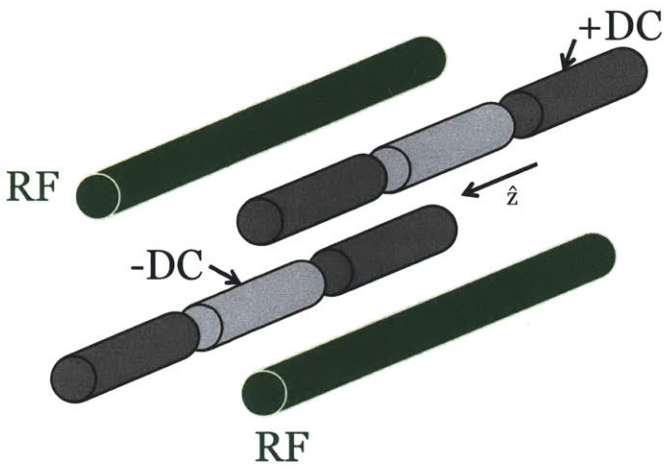

Figure 2-2: The electrodes of a linear Paul-trap. The ideal rod geometry is hyperbolic but it is far easier to construct the trap with four rods. The RF field at the center is quadrupolar. The DC electrodes are split into positive (black) and negative (gray) provide confinement along the trap axis $\hat{z}$.

shown in Figure 2-2 as

$$\phi(x, y, z, t) = \phi_{\mathrm{dc}}(x, y, z) + \phi_{\mathrm{rf}}(x, y, z) \cos \omega_{\mathrm{rf}} t \,, \tag{2.1}$$

where ω_{rf} is the radial frequency of the signal on the RF electrodes.

The combination of the RF and DC potentials in Eq. 2.1 are simplified using three assumptions. The first assumption is that both the RF and DC trapping potentials are separable, namely $\phi(x, y, z) = \phi(x) + \phi(y) + \phi(z)$[10, 12]. The second assumption is that the potential is well approximated by a polynomial of second order. Lastly, the DC and RF polynomials are assumed to be centered on the same point in space (x_0, y_0, z_0). The combination of these three assumptions leads to

$$\begin{aligned} \phi(x, y, z, t) = & \frac{1}{2}\left(c_{\mathrm{x}}(x - x_0)^2 + c_{\mathrm{y}}(y - y_0)^2 + c_{\mathrm{z}}(z - z_0)^2\right) + \\ & \frac{1}{2}\left(\gamma_{\mathrm{x}}(x - x_0)^2 + \gamma_{\mathrm{y}}(y - y_0)^2 + \gamma_{\mathrm{z}}(z - z_0)^2\right) \cos(\omega_{\mathrm{rf}} t) \,. \end{aligned} \tag{2.2}$$

There is no loss of generality by defining the center of the trap at the origin, $(0, 0, 0)$.

The potential in Eq. 2.2, derived from the assumptions about Eq. 2.1, must still satisfy Laplace's equation which requires that the divergence of the DC and RF electric fields must be zero at all times. This requirements places constraints on the coefficients in Eq. 2.2. The divergence of the electric field is given by the Laplacian of the potential in Eq. 2.2

$$\nabla^2\phi(x,y,z,t) = c_x + c_y + c_z + (\gamma_x + \gamma_y + \gamma_z)\cos\omega_{rf}t = 0\,. \tag{2.3a}$$

Therefore we can write that

$$c_x + c_y + c_z = 0 \quad \text{and} \tag{2.3b}$$

$$\gamma_x + \gamma_y + \gamma_z = 0\,. \tag{2.3c}$$

The geometry of the electrodes also constrains the values of the coefficients in Eq. 2.2. The DC electrodes confine in the z direction, and the coefficients in the x and y directions are equal because of the symmetry of the electrodes. Therefore

$$c_z = -(c_x + c_y) = -2c_x = -2c_y\,. \tag{2.4}$$

Also, the RF electrodes cannot confine in the z direction because the DC electrodes put the ions at the center of the rods in Figure 2-2. Therefore the RF coefficient in the z direction must be zero and we can write that

$$\gamma_x = -\gamma_y\,,\ \gamma_z = 0\,. \tag{2.5}$$

After calculating and simplifying the potential around the trap center it is possible to determine the equations of motion for an ion placed in the trapping potential given by Eq. 2.2.

2.1.1 Equations of Motion

The equations of motion for ions in a quadrupole trap lead to solutions that include resonances. Mass spectroscopy uses these resonances in order to determine which ion species are present in ion traps. This section outlines the mathematics governing the ion motion in the trapping potential applied by the ion trap.

The forces exerted by the trapping potential on an ion of mass m can be written as the charge Ze times the electric field generated by the applied voltages. Since the potential in Eq. 2.2 was separable, the equation of motion in each direction follows the same form and each direction can be analyzed in the same way. Therefore, I will only consider the equation in the x direction which is

$$m\ddot{x} = -Zex\left(c_{\mathrm{x}} + \gamma_{\mathrm{x}}\cos(\omega_{\mathrm{rf}}t)\right) . \tag{2.6}$$

The equation of motion in Eq.2.6 is the same as the Mathieu equation

$$\frac{d^2x}{d\xi} + \left(a_{\mathrm{x}} - 2q_{\mathrm{x}}\cos(2\xi)\right)x = 0\,, \tag{2.7}$$

under the following variable substitutions

$$\begin{aligned} \xi &= \frac{\omega_{\mathrm{rf}}t}{2} \\ a_{\mathrm{x}} &= \frac{4Zec_{\mathrm{x}}}{m\omega_{\mathrm{rf}}^2} \\ q_{\mathrm{x}} &= \frac{2Ze\gamma_{\mathrm{x}}}{m\omega_{\mathrm{rf}}^2}\,. \end{aligned} \tag{2.8}$$

a_{x} and q_{x} are referred to as the stability parameters of the trap in the x direction. The general solution to the Mathieu equation is well known[12], however this general form is beyond the scope of this thesis. It is important to note that the solution to the Mathieu equation is not stable for all values of a and q, thus additional requirements on the RF and DC coefficients in Eq. 2.2 are necessary for the ion motion to be confined.

A range of a and q parameters for which the solution to the Mathieu equation

is stable is a stability region. All of the ion traps in this experiment operate in the stability region that contains the point $(a_x = 0, q_x = 0)$, which is called the lowest stability region.

There are three a and q parameters for a given trap design, one set for each direction. The constraints imposed by Eqs. 2.4 and 2.5 reduce the number of a and q parameters. The static requirements in Eq. 2.4 require

$$a_z = -(a_x + a_y) = -2a_x = -2a_y \,. \tag{2.9}$$

Similarly, the requirements on the RF electrodes in Eq. 2.5 require

$$q_x = -q_y \,,\, q_z = 0 \,. \tag{2.10}$$

The stability of the Mathieu equation in the x direction is dependent on the characteristic exponent β, which is a function[1] of only a_x and q_x[12]. In the lowest stability region β_x is approximately given by

$$\beta_x \approx \sqrt{a_x + q_x^2/2} \,. \tag{2.11}$$

When β is real valued in all directions the ion will be completely confined. The lowest stability region for the linear Paul-trap is shown in Figure 2-3.

In a stable trap the motion of ions will have two different frequency components; one corresponds to the applied RF frequency and the other to the characteristic exponent β times the RF frequency. The RF motion is referred to as micro-motion and is usually ignored in the treatment of ion motion and confinement. The motion corresponding to β is the secular motion of the trap which can be approximated by the pseudopotential[10]. In our traps the RF frequency is 6 MHz and the secular motion frequency is between 100 kHz and 1 MHz depending on the amplitude of our voltage signals.

[1]Solutions to the Mathieu equation are so well known that software packages such as Mathematica have built in functions, like MathieuCharacteristicExponent[a,q], to calculate β

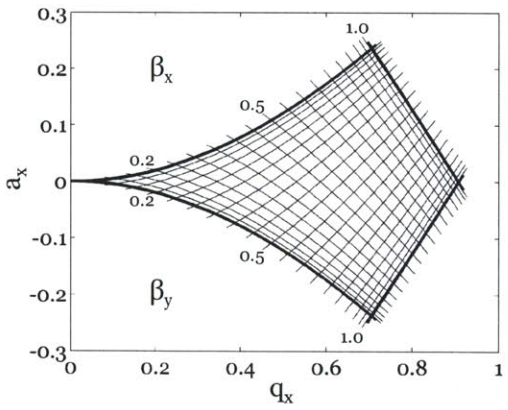

Figure 2-3: The stability diagram for the lowest region in the linear Paul-trap where $q_x = -q_y$, so that either positive or negative values of a_x are possible. The values of β are calculated using MathieuCharacteristicExponent in Mathematica and not the approximation.

2.1.2 Pseudopotential

The pseudopotential is a powerful tool for analyzing the motion of an ion in a stable trap. It allows us to simplify the forces exerted on the ion into static terms, which provides for easier simulation and visualization of the trapping potential. This static confinement makes it possible to estimate the energy required for an ion to escape from the trap, or the trap depth. In Chapter 3, I apply this concept to the surface electrode ion traps that we use in our experiment.

The pseudopotential is given by

$$\begin{aligned} \psi(x,y,z) &= \frac{Z^2e^2}{4m\omega_{\mathrm{rf}}^2}|\nabla\phi_{\mathrm{rf}}|^2 = \frac{Z^2e^2}{4m\omega_{\mathrm{rf}}^2}\left(\gamma_x^2x^2+\gamma_y^2y^2+\gamma_z^2z^2\right) \\ &= \gamma_x'x^2+\gamma_y'y^2+\gamma_z'z^2\,. \end{aligned} \tag{2.12}$$

The pseudopotential is fast to calculate, although it is limited in accuracy. The actual trap depth can be as much as 20% different and more powerful tools, such as CPO from Simion[2], are required to get more accurate information.

[2]http://simion.com/cpo/

2.2 Applications of Ion Traps

The above section looked at ion motion and stable ion confinement. This section examines applications of ion traps including mass spectroscopy, laser cooling and ion crystallization. Mass spectroscopy is used in our experiment to verify the presence of both Sr^+ and $SrCl^+$ ions in our trap. Laser cooling is used to lower the temperature of the ion cloud and the re-emitted photons from the cooling process allow us to detect changes in the temperature of the cloud. Ion crystallization may be used in future experiments in our group to increase the sensitivity of our measurement of sympathetic heating of the Sr^+ ions.

2.2.1 Mass (Tickle) Spectroscopy

In our experiment we use mass spectroscopy to verify that Sr^+ and $SrCl^+$ are present in the trap. Both Sr^+ and $SrCl^+$ ion species are required in order to perform our experiment. This section explains which features of the equation of motion make a mass spectroscopy scan possible.

The trapping potential in Eq. 2.2 is quadratic and therefore, the forces exerted on the ions in the trap are linear restoring forces. Such linear restoring forces lead to resonances that can be driven by the application of a small amplitude signal added to the DC electrodes, sometimes called a tickle signal. There are three resonant frequencies of ions in a linear Paul-trap that depend on the coefficients in Eq. 2.2. The resonant frequency in the z direction is the axial secular frequency, while the resonant frequencies in the x and y directions are the radial secular frequencies.

The resonant frequency in the z direction can be found from β_z. Combing Eq. 2.11 and 2.10, β_z is given by

$$\beta_z \approx \sqrt{a_z + q_z^2/2} = \sqrt{a_z}\,. \tag{2.13}$$

When the tickle signal frequency is the same as the resonant frequency given by

$$\begin{aligned} \omega_t &= \frac{\beta_z \omega_{rf}}{2} = \sqrt{\frac{4Zec_z}{m\omega_{rf}^2}} \frac{\omega_{rf}}{2} \\ &= \sqrt{\frac{Zec_z}{m}}, \end{aligned} \tag{2.14}$$

the ion motion will grow rapidly. This resonant frequency is mass dependent which makes it possible to measure the mass of ions in the trap.

Unlike the axial frequency, the radial secular frequencies are dependent on both the DC and RF confinement. Because of the RF confinement, the q value in Eq. 2.11 cannot be dropped from the equation, complicating the relationship between resonant frequency and mass. Therefore, mass spectroscopy scans usually excite the axial resonant frequency instead of the radial resonant frequencies.

2.2.2 Laser Cooling and Imaging

Laser cooling by the Doppler effect lowers the temperature of the ions in the trap and generates a signal for imaging the ions that is dependent on temperature. We use the temperature dependence of ion fluorescence to look for heating in the trap. We expect to see heating in the trap when we drive rotational transitions in $SrCl^+$.

Trapped ions are cooled using a laser tuned below an allowed electronic transition. An ion speeding towards the laser will experience a higher frequency because of the Doppler effect, increasing the probability that the ion will absorb the incoming photon. This photon will reduce the momentum of the ion by $\Delta p = \hbar k$ and therefore reduce the kinetic energy of the ions in the trap.

Atoms can often decay into a different state than they started in, which makes laser cooling less effective. For example the ground state of Sr^+ is the $5^2S_{1/2}$ state and a cooling transition excites the ion into the $5^2P_{1/2}$ state which can decay into the $4^2D_{3/2}$ or the $5^2S_{1/2}$ state. The level diagram illustrating these states is shown in Figure 2-4. In order to keep the cooling process efficient, a second laser is used to re-pump Sr^+ from the long-lived $4^2D_{3/2}$ back into the $5^2P_{1/2}$.

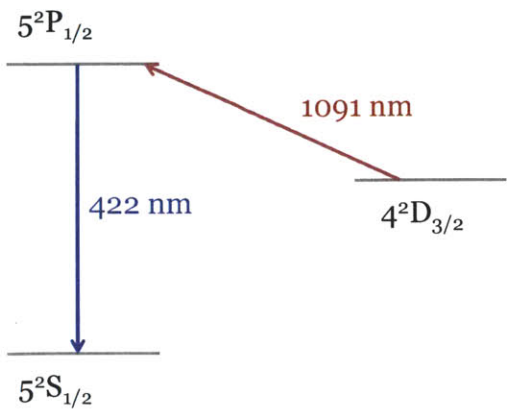

Figure 2-4: Sr^{88} level diagram for Doppler cooling where the wavelength of the cooling laser is 422 nm and the wavelength of the re-pump laser is 1091 nm.

The re-emitted photons from the cooling process can be collected in order to image the ions in the trap. As the ions cool, it is possible to reduce the detuning from the true resonant frequency, which increases the rate for photons to be absorbed and re-emitted. When the laser is properly tuned, the fluorescence of the ions is a probe of the temperature of the ion cloud. If the ions are excited to a higher temperature, for example by a tickle spectroscopy signal, then the fluorescence will decrease.

2.2.3 Ion Crystallization

Laser cooling can lower the temperature of ions to a point where we can study interactions that only occur at ultra-cold temperatures, such as ion crystallization. At ultra-cold temperatures, the laser detuning is so small that fluorescence from crystallized ions is more sensitive than ions in a cloud state to spurious heating within the trap. Therefore, ion crystals may provide our group with more sensitive tools for future experiments.

When the ions are cold enough they will condense into a crystal where the spacing between the ions is dependent on their charge and the strength of the confining potential[11]. A large crystal is shown in Figure 2-5(a). The ion sites are arranged so that the Coulomb repulsion counters the confinement from the electrodes. The

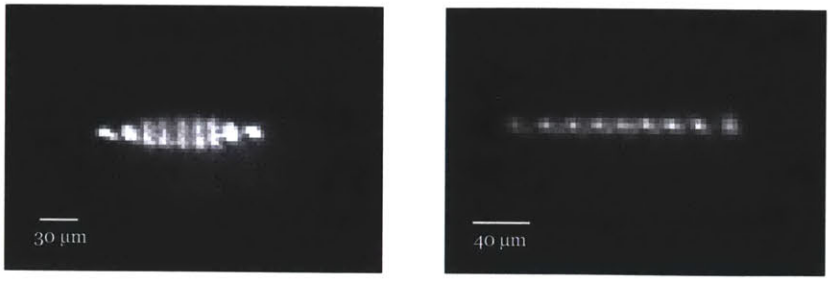

(a) (b)

Figure 2-5: Ion crystals in surface electrode traps with a 3-D crystal (a) and a linear crystal (b). Both of these crystals are Sr^+ ions and the typical spacing from one ion to another is approximately 20 µm. These crystals were formed in the White Sox1C trap that is discussed in Chapter 6.

confinement in linear Paul-traps defined in Eq.2.2 makes it possible to confine the ions more tightly with the RF electrodes than the DC electrodes to make a 1-D ion crystal as shown in Figure 2-5(b).

Chapter 3

Surface-Electrode Ion Traps

This chapter takes the methods of analysis for ion traps presented in the last chapter and applies the same methods to the specific geometry of our surface-electrode ion traps. We use these types of traps because the geometry is consistent with coplanar waveguide transmission lines which we require to generate microwave electric fields that drive rotational transitions in $SrCl^+$ molecular ions. We use the pseudopotential and the stability parameters to calculate the properties of Sr^+ and $SrCl^+$ inside our ion traps which allows us to predict the secular frequencies of each species of ion. Predicting the secular frequencies allows us to perform accurate mass spectroscopy and verify that we have both ion species present in our traps.

3.1 Electrode Geometry and the Potential from a Single Electrode

The linear quadrupole ion traps discussed in Chapter 2 are the precursors to the surface-electrode ion traps used in our experiment. This section first illustrates the geometry of the surface-electrode ion traps and then calculates the electric potential from a single square electrode. The linearity of the electric potential makes it possible to use this formula to write down the total trapping potential and the pseudopotential later in this chapter.

Figure 3-1: The basic configuration of electrodes for a surface-electrode trap. The green electrodes are the two RF signals and the black electrode is DC. This geometry is also consistent with the coplanar waveguide transmission line.

Two RF electrodes in a surface-electrode ion trap generate an approximate quadrupole field by placing a third electrode with a DC bias between the RF electrodes as shown in Figure 3-1. The surface-electrode geometry is similar to the four electrode geometry of the linear Paul-trap except that the second DC electrode is placed at infinity.

One advantage of surface-electrode traps is that they can be prototyped quickly and fabricated with the same techniques used in the semi-conductor industry[5, 19]. Another advantage of the surface-electrode trap is that a coplanar-waveguide transmission line can be incorporated into the center of the trap into the ion trap with minimal changes to the electrode geometry. We use this property of surface-electrode traps to bring in microwave signals to drive rotational transitions in trapped polar molecular ions.

In this chapter, I discuss the changes that must be made to the simple structure in Figure 3-1 to confine an ion in all directions. I also outline the process for calculating the DC and RF potentials used to calculate the stability parameters like those in the last chapter. Lastly, I discuss the code available in Appendix B.1 that calculates the stability for Sr^+ and $SrCl^+$ for the specific traps used in our experiment (which were all named after U.S. major league baseball teams).

The geometry in Figure 3-1 is translationally invariant, similar to the RF electrodes in the linear Paul-trap in Chapter 2. Therefore an ion cannot be confined in the direction parallel to the electrodes, which is the axial direction. Additional DC electrodes are placed outside of the RF electrodes and biased to confine the ions in

Figure 3-2: The five-wire surface-electrode trap configuration with additional DC electrodes placed on the outside of the RF so confine an ion along the three electrodes from Figure 3-1.

the axial direction. This geometry is shown in Figure 3-2 and is called the "five-wire geometry"[5] because it has five electrodes in the cross section; starting with DC, then RF, then DC, then RF, and finally DC.

We added ten additional DC electrodes to the outside of the RF electrodes, five on each side. The labels of the additional DC electrodes shown in Figure 3-2 show that we applied three voltage levels. We applied one level to the four corner electrodes that define the outside of the trapping zone, or ends. We applied another level to the two electrodes at the center of the trapping zone, or middle electrodes. We also applied one level to the remaining four electrodes that were between each end and mid, called quad electrodes.

The potential for every electrode in our ion traps can be calculated with the formula derived by M.G. House[10]. This formula calculates the potential of a square electrode at voltage V with two opposite corners at coordinates $(x_1, 0, z_1)$ and $(x_2, 0, z_2)$, such that the potential on the $y = 0$ surface is given by

$$\phi(x, 0, z) = \begin{cases} V & x_1 < x < x_2 \;\&\; z_1 < z < z_2 \\ 0 & \text{otherwise.} \end{cases} \tag{3.1}$$

For the calculation to work the potential must reduce to zero as $y \to \infty$ and it must

be finite for $x \to \pm\infty$ and $z \to \pm\infty$. The general solution for this potential is

$$\begin{aligned}\phi(x,y,z) = \frac{V}{2\pi}\Bigg\{ &\arctan\left(\frac{(x_2-x)(z_2-z)}{y\sqrt{y^2+(x_2-x)^2+(z_2-z)^2}}\right) \\ &- \arctan\left(\frac{(x_1-x)(z_2-z)}{y\sqrt{y^2+(x_1-x)^2+(z_2-z)^2}}\right) \\ &- \arctan\left(\frac{(x_2-x)(z_1-z)}{y\sqrt{y^2+(x_2-x)^2+(z_1-z)^2}}\right) \\ &+ \arctan\left(\frac{(x_1-x)(z_1-z)}{y\sqrt{y^2+(x_1-x)^2+(z_1-z)^2}}\right)\Bigg\}.\end{aligned} \tag{3.2}$$

3.2 Matlab Simulations of Giants7

The potential in Eq. 3.2 can be applied to the DC and RF electrodes which makes it possible to analytically calculate the potential at the center of the ion trap in Figure 3-2. This analytic formula can be used to calculate the pseudopotential or the Mathieu stability parameters. The stability parameters are found by numerically approximating Eq. 3.2 as a polynomial of second order around the trap center. The rest of this chapter focuses on simulation results from Matlab.

3.2.1 Isosurface Plot

The Matlab code in Appendix B.1 calculates the pseudopotential for the surface-electrode ion traps used in our experiment. The simulation for Giants7 was also applied to the White Sox and Cubs traps. We applied the same simulation for all three traps because each trap had the same trapping electrodes. The difference between each trap series was their microwave characteristics.

We used this Matlab code to calculate the pseudopotential, the secular frequencies and the stability parameters as a function of the applied voltages in Table 3.1 to the electrodes in Giants7. An isosurface of the pseudopotential calculated with the code is shown in Figure 3-3.

Electrode	Voltage (V)
Ends	+21
Quads	0
Mids	-30
RF	500[a]
Microwave	0

[a] zero-peak voltage

Table 3.1: Applied voltages for simulation of Giants7. The voltages were applied symmetrically so the four end electrodes were all at the same voltage, the four quads were at the same voltage and the four mids were at the same voltage.

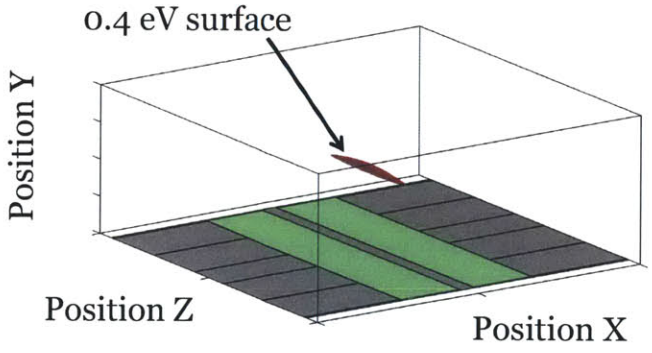

Figure 3-3: Simulated trap structure for Giants7 from the code in Appendix B.1. Since the surface is closed the ion is contained with greater than 0.4 eV in this simulation. The trapping site was moved 1.2 mm higher in the y-direction so that it would be easier to see in this figure.

Species	a	q	β
Strontium	0.001065	-0.003351	0.0327203
	-0.002835	0.627401	0.484436
	0.001766	-0.629651	0.492945
Strontium Chloride	0.000762	-0.002395	0.0276563
	-0.002027	0.448481	0.327737
	0.001263	-0.450089	0.334648

Table 3.2: Stability parameters for Giants7 calculated using the voltages in Table 3.1. a and q are the stability parameters from the Mathieu Equation in Eq. 2.7 and β is the characteristic exponent that is a function of a and q calculated in Mathematica. If $0 \leq \beta \leq 1$ and $\beta \in \Re$ then the trap is stable in the lowest stability region.

3.2.2 Stability Parameters of Giants

Unless both atomic and molecular ion species are stable in our traps, our experiment will fail. Therefore, we ran a simulation of the trap using typical voltages applied to the electrodes during the experiment to make sure that the ions were stable. Also, as we change the voltages on the electrodes, the stability will change so the code in Appendix B.1 can be used to verify that we have not moved to an unstable region in the $a - q$ plane for $SrCl^+$ (which we cannot see with our camera).

The stability parameters for Giants7 are not symmetric like those in the linear Paul-trap in Section 2.1.1. However, we can still calculate the characteristic exponent (β) which determines stability in all three directions. If the trap is unstable in any one direction for either Sr^+ or $SrCl^+$ then our experiment will not work. The stability parameters in all three directions for both Sr^+ and $SrCl^+$ were calculated using the voltages in Table 3.1 and the results are reported in Table 3.2.

Chapter 4

Coplanar Transmission Lines

In order to drive rotational transitions in $SrCl^+$ we must integrate a microwave transmission line into the surface-electrode ion traps. Coplanar waveguide (CPW) transmission lines can be integrated into the traps with minimal changes to the electrodes. In this chapter I present the mathematics governing the waves of voltage and current on a transmission line, then I apply this math to our CPW transmission line. I then discuss the characteristic impedance and the propagation constant for CPW transmission lines. These values determine the behavior of the voltage and current present near the ions in our experiment. Knowing the voltage of the center conductor of the CPW line allows us to calculate the electric field that the $SrCl^+$ ions experience, which determines the rate at which we can drive rotational transitions in $SrCl^+$. This rate establishes how much heat the Sr^+ ion cloud will experience[2], and if there is enough heating we will be able to detect a temperature change.

4.1 Transmission Lines

The success of our experiment relies on sending approximately 1 W of microwave signals into our ion traps to efficiently drive the rotational transitions of $SrCl^+$. The most efficient method of transmitting these high-power microwave signals is through integrated transmission lines. This section outlines the mathematics governing transmission lines.

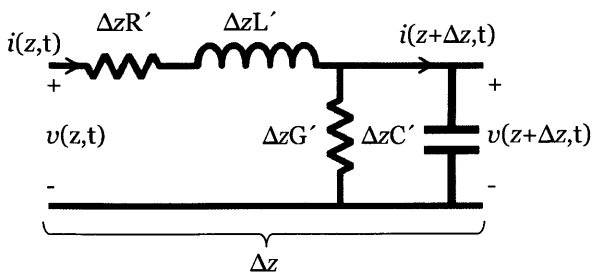

Figure 4-1: The circuit elements of an infinitesimal length of transmission line of length Δz

Transmission lines exist at the divide between circuit theory and the electromagnetic fields that carry AC electrical signals. This section will analyze a generic transmission line using a series of lumped element circuit components in order to derive the voltage and current on a transmission line. The voltage and current are dependent on the characteristic impedance and propagation constant of the transmission line as well as the reflections possible from impedance mismatches that we will deal with in our transmission lines.

There are four circuit parameters that characterize the voltage and current on a transmission line: capacitance per unit length C', inductance per unit length L', resistance per unit length R' and conductance per unit length G'. Transmission line analysis begins by analyzing the circuit for an infinitesimal line of length Δz which combines these four parameters to form the circuit in Figure 4-1.

The circuit in Figure 4-1 is analyzed with Kirchhoff's voltage and current laws which results in the following formulas for the voltage and current[18]

$$v(z,t) - R'\Delta z i(z,t) - L'\Delta z \frac{\partial i(z,t)}{\partial t} - v(z+\Delta z,t) = 0 \tag{4.1a}$$

and

$$i(z,t) - G'\Delta z v(z+\Delta z,t) - C'\Delta z \frac{\partial v(z+\Delta z,t)}{\partial t} - i(z+\Delta z,t) = 0\,. \tag{4.1b}$$

The first step in in solving these equations is to separate the spatial dependence from

the time dependence and apply phasor analysis. Phasor analysis allows the voltage to be written $v(z,t) = \Re\left(V(z)e^{-\jmath\omega t}\right)$ with a similar relation for the current. Phasor analysis simplifies the time derivatives to

$$\frac{\partial v(z,t)}{\partial t} = -\jmath\omega v(z,t)\,. \tag{4.2}$$

Because every term in Eq. 4.1a and 4.1b has the term $e^{-\jmath\omega t}$, $e^{-\jmath\omega t}$ can be dropped thus removing time dependence.

The next step to solve for the voltage and current in a transmission line is to take the limit $\Delta z \to 0$. The resulting relations are

$$\frac{dV(z)}{dz} = -(R' + \jmath\omega L')I(z) \quad \text{and} \tag{4.3a}$$

$$\frac{dI(z)}{dz} = -(G' + \jmath\omega C')V(z)\,. \tag{4.3b}$$

These two equations are known as the Telegrapher's Equations. The solutions to Eq. 4.3 are forward and backward propagating waves for both the current and the voltage. These equations are

$$V(z) = V_+e^{-\gamma z} + V_-e^{\gamma z} \tag{4.4a}$$

and

$$I(z) = I_+e^{-\gamma z} + I_-e^{\gamma z} = \frac{1}{Z_0}\left(V_+e^{-\gamma z} - V_-e^{\gamma z}\right)\,, \tag{4.4b}$$

where $\gamma = \sqrt{(R' + \jmath\omega L')(G' + \jmath\omega C')} = \alpha + \jmath\beta$ is the propagation constant and Z_0 is the characteristic impedance given by

$$Z_0 = \sqrt{\frac{R' + \jmath\omega L'}{G' + \jmath\omega C'}}\,. \tag{4.5}$$

This β should not be confused with the characteristic exponent from the analysis of ion trapping.

The Telegrapher's Equations apply to all transmission lines but can be simplified for lossless lines where $G' = R' = 0$. After this simplification, the propagation

constant $\gamma = \jmath\omega\sqrt{L'C'}$ and is therefore purely imaginary, while the characteristic impedance $Z_0 = \sqrt{\frac{L'}{C'}}$ and is therefore purely real.

The characteristic impedance of the microwave source network is $50\,\Omega$, but the transmission lines in our trap will not be matched to this standard impedance. Impedance mismatches are important because reflections at the beginning of our CPW lines in our trap will reduce the electric field at the ions, which lowers the potential heating rate from driving the rotational transitions. The voltage reflection from our trap is dependent on the input impedance (Z_{in}) of our transmission lines, as given by

$$\Gamma = \frac{50 - Z_{\text{in}}}{50 + Z_{\text{in}}}. \tag{4.6}$$

The input impedance is given by

$$Z_{\text{in}}(-\ell) = Z_0 \frac{50 + \jmath Z_0 \tan(\beta\ell)}{Z_0 + \jmath 50 \tan(\beta\ell)}. \tag{4.7}$$

The convention is to use $-\ell$ instead of ℓ because it is assumed that the load is at point $z = 0$ and that the transmission line runs in the $-z$ direction. The load of the trap transmission line is the same as the source impedance of $50\,\Omega$ and when $\tan(\beta\ell) = 0$ the input impedance can be matched to the impedance of the microwave source. This impedance match occurs regardless of the characteristic impedance of our CPW transmission lines.

4.2 Coplanar Waveguide Transmission Lines

The advantage of a CPW line for this project is that it can be integrated into our surface electrode ion traps with minimal changes to the geometry. One drawback, however, is that the dielectric layer exposed to the ion will have static charge build-up on the surface. This charge will alter the DC trapping potential calculated in Chapter 3, potentially moving the ions into unstable conditions of the Mathieu parameters. To combat this problem the exposed dielectric of the CPW must be minimized, which will effect the characteristic impedance of the transmission line and create undesirable

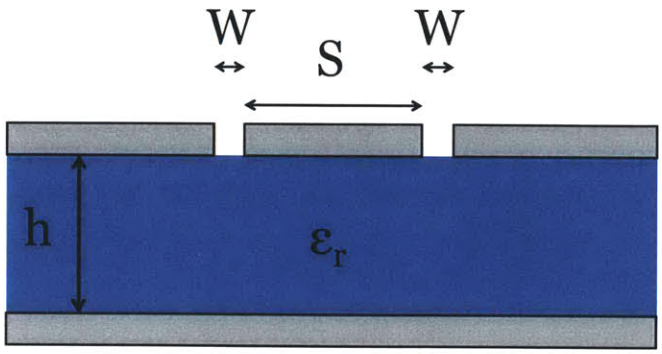

Figure 4-2: Cross-section of a ground backed CPW transmission line where S is the width of the center electrode, W is the width of the gap, h is the thickness of the dielectric and ε_r is the dielectric constant

reflections in our microwave network.

The specific type of transmission line we use in our experiment is the coplanar waveguide (CPW) transmission line which consists of a finite width center conductor with semi-infinite ground planes on both sides. The CPW lines used in this project also have a ground plane on the reverse side of the dielectric as shown in Figure 4-2. This geometry is sometimes referred to as the conductor-backed CPW or CBCPW. Since conductor backed geometry is the only geometry used in the project I will just refer to it as the CPW geometry.

4.2.1 Characteristic Impedance

The characteristic impedance impacts possible reflections within our microwave network which could reduce how efficiently we could send high-power signals into the traps.

The characteristic impedance of a CPW transmission line is dependent on the three geometric factors shown in Figure 4-2; S is the width of the center electrode, W is the width of the gap and h is the thickness of the dielectric. These geometric

factors determine the capacitance per unit length and the inductance per unit length which are calculated using conformal mapping[21]. The capacitance per unit length is

$$C' = 2\varepsilon_0\varepsilon_{\text{eff}}\left(\frac{K(k)}{K(k')} + \frac{K(k_1)}{K(k_1')}\right), \tag{4.8}$$

where ε_{eff} is the effective dielectric constant for the line given by

$$\varepsilon_{\text{eff}} = \frac{1 + \varepsilon_{\text{r}}\frac{K(k')}{K(k)}\frac{K(k_1)}{K(k_1')}}{1 + \frac{K(k')}{K(k)}\frac{K(k_1)}{K(k_1')}}. \tag{4.9}$$

The inductance per unit length is

$$L' = \frac{\mu_0}{2}\frac{1}{\frac{K(k)}{K(k')} + \frac{K(k_1)}{K(k_1')}}. \tag{4.10}$$

$K(k)$ is the complete elliptic integral of the first kind while the values of the arguments k, k_1, k' and k_1' are given by:

$$k = \frac{S}{S + 2W}, \tag{4.11a}$$

$$k_1 = \frac{\tanh\left(\frac{\pi S}{4h}\right)}{\tanh\left(\frac{\pi(S+2W)}{4h}\right)}, \tag{4.11b}$$

$$k' = \sqrt{1 - k^2}, \tag{4.11c}$$

$$k_1' = \sqrt{1 - k_1'^2}. \tag{4.11d}$$

The capacitance and inductance per unit length can be used to calculate the characteristic impedance Z_0 which is given by

$$Z_0 = \sqrt{\frac{L'}{C'}} = \sqrt{\frac{\mu_0}{4\varepsilon_0\varepsilon_{\text{eff}}}}\frac{1}{\frac{K(k)}{K(k')} + \frac{K(k_1)}{K(k_1')}}. \tag{4.12}$$

This characteristic impedance can be modified due to the finite thickness of the conductors on the top plane in Figure 4-2. However, these modifications produce a negligible correction for our devices. The correction is proportional to the ratio of the

Geometric Factor	Value
S	400 µm
W	25 µm
h	500 µm
ε_r	10

Table 4.1: The CPW transmission lines in our experiment were the same in the Giants series and the White Sox chips. S is the width of the center electrode, W is the width of the gap between the electrodes, h is the height of the dielectric and ε_r is the dielectric constant. Sapphire is anisotropic, but the wafers we purchase can be approximated as isotropic with a relative dielectric constant of 10

thickness of the top metal layer to the width of the center line and the thickness of the dielectric. The thickness of the metal layer in our devices was between 200 nm and 400 nm while the center conductors were 400 µm wide and the substrate was 500 µm so the ratios are less than 0.001.

The characteristic impedance of our CPW line that we used is 28.6 Ω and effective dielectric constant is 5.65, as calculated using the parameters in Table 4.1. As mentioned before our CPW lines are in the middle of two 50 Ω microwave networks.

The voltage on the center conductor of the CPW line is dependent on the difference in the characteristic impedance Z_0 from the 50 Ω network. These differences will cause reflections that will vary the voltage on the center conductor. A voltage wave on the CPW line has a reflection coefficient given by

$$\Gamma_r = \frac{28.6 - 50}{28.6 + 50} = -0.27\,. \tag{4.13}$$

This reflection coefficient creates voltage standing wave on our CPW lines so that ion location becomes important in determining the electric field that the ion cloud experiences. If the voltage on the CPW line would have been 1 V then the actual voltage on the chip will vary between 0.73 and 1.27 V due to these reflections.

4.2.2 Propagation Constant

The propagation constant of the CPW transmission line determines the wavelength of the waves of voltage and current on the transmission line. By properly designing

the length of our CPW transmission line, such that $\tan(\beta\ell) = 0$, we can maximize the power transfer. The propagation constant also determines the amount of loss present in the CPW transmission line within the trap. This loss can cause heating of the niobium layer and may cause the transmission line to transition from superconducting to a normal metal.

The imaginary part of the propagation constant β is given by

$$\beta = \omega \frac{1}{\sqrt{L'C'}} = \frac{\omega}{\sqrt{\varepsilon_{\text{eff}}\varepsilon_0\mu_0}} = \frac{\omega c}{\sqrt{\varepsilon_{\text{eff}}}}, \tag{4.14}$$

where c is the speed of light in vacuum. This value determines the wavelength of the signal at frequency ω. If we choose our transmission lines to be an integer number of half-wavelengths, we maximize the power transmitted into the CPW waveguide. Therefore, we can maximize the heating rate of the trapped ion cloud.

Small amounts of loss on a transmission line can be incorporated into an attenuation constant, α which ignores the effect of the lossy transmission line on the characteristic impedance or β. The attenuation constant for the CPW transmission line is usually broken into two components $\alpha = \alpha_{\text{d}} + \alpha_{\text{c}}$ where α_{d} is the loss due to the dielectric and α_{c} is the loss due to the conductors.

The dielectric loss is given by[21]

$$\alpha_{\text{d}} = \frac{\pi\varepsilon_{\text{r}}}{\lambda_0\sqrt{\varepsilon_{\text{eff}}}} \frac{\varepsilon_{\text{r}} - 1}{\varepsilon_{\text{eff}} - 1} \tan\delta_{\text{e}}, \tag{4.15}$$

where $\tan\delta_{\text{e}}$ is the loss tangent for the dielectric substrate. Sapphire is a low-loss dielectric, therefore α_{d} is negligible. However, this loss becomes important when dealing with superconducting transmission lines such as CPW lines we integrated with our ion traps.

The calculation for the conductor losses in a standard CPW geometry provides an approximation for the losses in a conductor-backed CPW. The conductor loss for a standard CPW without the back conductor is given by[21]

$$\alpha_{\text{c}} = \frac{R_{\text{c}} + Rg}{2Z_0}, \tag{4.16}$$

where R_c is the resistance per unit length of the center conductor and R_g is the resistance per unit length of the top ground planes. R_c and R_g are given by

$$R_c = \frac{R_s}{4S(1-k^2)K^2(k)}\left\{\pi + \ln\left(\frac{4\pi S}{t}\right) - k\ln\left(\frac{1+k}{1-k}\right)\right\} \tag{4.17a}$$

and

$$R_g = \frac{kR_s}{4S(1-k^2)K^2(k)}\left\{\pi + \ln\left(\frac{4\pi(S+2W)}{t}\right) - \frac{1}{k}\ln\left(\frac{1+k}{1-k}\right)\right\}. \tag{4.17b}$$

R_s is the surface resistance of the metal, k is the same as defined in Eq. 4.11a and t is the thickness of the metal layer. The surface resistance can come from the finite conductivity of the normal metal given by[21]

$$R_s = \sqrt{\frac{\omega\mu}{2\sigma}}, \tag{4.18}$$

where ω is the operating frequency, μ is the permeability of the conductor and σ is the conductivity. R_s can also come from the real part of the complex surface resistance of a superconductor[15, 8, 14].

The attenuation constant for the CPW waveguide is dependent on temperature and frequency but is approximately 0.01 Np/m for typical experimental conditions. The attenuation constant is important because the attenuated power is converted into heat that must be dissipated into the cryostat. If the cryostat cannot pull heat away fast enough the temperature of the electrodes on the trap will increase and possibly drive the niobium into the normal state. The attenuation constant of niobium in the normal state is high enough that the trap will warm considerably and impact the temperature of the ion cloud above, producing a false positive signal.

4.2.3 Electric Field

The CPW transmission line is used to bring microwave electric fields to the trapped molecular ions. This electric field is linearly proportional to the rate at which we can drive the rotational transitions of $SrCl^+$, and the faster we drive these rotations the

more the Sr^+ ion cloud will heat.

Electric fields generated by CPW transmission lines can be approximated using the same formula as the one in Chapter 3 for the field above a surface electrode. That formula relied on the quasistatic approximation, which is applicable in this situation because the ions are a few hundred micrometers above the surface of the trap while the wavelength in free-space is 4.5 cm, almost two orders of magnitude larger.

The calculation of the electric field is geometry dependent. Similar to the geometry of the surface-electrode trap the electrode is square with opposite corners at points $(x_1, 0, z_1)$ and $(x_2, 0, z_2)$, but in this calculation the electrode is assumed to have infinite extent in the z dimension. This approximation is valid because the center electrode is 400 µm wide and the ions are 600 µm above the electrode, while the transmission line is several centimeters long. The geometry of the CPW electrodes is symmetric in the x direction as shown in Figure 4-2 and so the origin is defined such that $x_1 = -S/2$ and $x_2 = S/2$.

The electric field at the ions is can be calculated by taking the gradient of the potential above the center electrode. This potential is given by

$$\phi(x,y) = \frac{V}{\pi}\left\{\arctan\left(\frac{(S-2x)}{2y}\right) + \arctan\left(\frac{(S+2x)}{2y}\right)\right\}. \tag{4.19}$$

Therefore the electric field above the surface of the CPW transmission line is given by

$$\begin{aligned}\vec{E} = -\nabla\phi = \frac{32Sxy}{S^4 - 8S^2(x^2-y^2) + 16(x^2+y^2)^2}\hat{x} + \\ \frac{4S(S^2 - 4x^2 + 4y^2)}{S^4 - 8S^2(x^2-y^2) + 16(x^2+y^2)^2}\hat{y}.\end{aligned} \tag{4.20}$$

Since the geometry of the CPW transmission line is symmetric about the center conductor, the electric field in the x direction reduces to zero.

Setting $x = 0$ in Equation 4.20 gives the electric field at the middle of the center electrode as

$$\vec{E} = \frac{V}{\pi}\frac{4S}{S^2 + 4y^2}\hat{y}. \tag{4.21}$$

Since the ions are trapped at about 600 µm with the center electrode 400 µm wide the electric field is $|E| = V \times 318\,\mathrm{m}^{-1}$. This approximation holds even though there is some modulation of the voltage on the line caused by the reflections because the modulation wavelength is over 1 cm. This length is several orders of magnitude larger than the electrode width and the ion height. A large electric field is critical in order to drive the rotational transitions quickly enough to heat the Sr^+ ion cloud.

Chapter 5

Fabrication and Experimental Apparatus

This chapter describes the fabrication process and experimental apparatus we used to design and test our traps. In order to maintain experimental design flexibility, we fabricated our own CPW transmission-line-integrated surface-electrode ion traps. This fabrication process involved niobium sputtering, direct-write lithography and etching. After fabricating the traps, we tested them in a closed cycle cryostat to see if our designs were capable of trapping ions and supporting high-power microwave signals. We took several thermal engineering steps to ensure that the Nb was superconducting. Heating caused by microwave losses when the Nb is not in the superconducting state would cause the same kind of heating we would have expected to see by driving rotational transitions of $SrCl^+$, thus resulting in a false positive.

In addition to careful thermal engineering, our testing apparatus has optical access for three lasers used to generate and trap ions, as well as access for the imaging network used to detect the ions. We also use a microwave amplifier network to source the signals that drive the rotational transitions in the polar molecular ions. In order to allow future researchers to replicate our results and understand the thought processes behind each design feature, this chapter contains part numbers and design tolerances as well as descriptions of the process.

5.1 Trap Fabrication

We fabricated our traps at MIT in the Nanostructures Laboratory[1] (NSL) using a niobium on sapphire process we developed[15]. We purchased the raw materials from suppliers as well as performed our own sputtering deposition and lithography so that we had full control over the variables that impact the trap quality. This fabrication process impacts the performance of the chips and it is important to understand what materials are used and why.

5.1.1 Niobium Sputtering

Our first step in fabricating the traps we used in our experiment was to sputter niobium (Nb) onto sapphire substrates. To do this, we used the Quantum Nanostructures and Nanofabrication group laboratory. We used a 99.95% pure Nb slug target from Alfa Aesar[1] and sapphire substrates from MTI Corporation[2] because these materials have been used by other groups to fabricate high quality superconducting ion traps[23] and microwave devices[14].

Our sapphire wafers were 2 inch diameter, 0.5 mm thick C-Plane sapphire substrates that were epitaxially polished on one side. We deposited the Nb onto these using DC magnetron sputtering in a Model ATC 2000 thin film deposition system built by AJA[3].

Before we sparked the DC plasma for sputtering, we flushed the gas lines feeding the AJA to remove possible contaminants. Then we cleaned the Nb target by sputtering away the top surface onto a closed shutter for three minutes. We then sputtered the Nb onto the epitaxially smooth surface of the wafer, which was fixed 18 cm from the Nb target and rotated at 50 rpm. The sputtering chamber pressure was held at 3 mTorr during the sputtering process and the current of the plasma was 300 mA. Under these conditions the Nb was deposited at 2.7 nm/min as measured by

[1] http://nanoweb.mit.edu
[1] http://www.alfa.com/
[2] http://www.mtixtl.com/
[3] http://www.ajaint.com/

a quartz oscillator inside the chamber. We sputtered the wafers for 75 to 150 minutes for total Nb thickness between 200 and 400 nm.

5.1.2 Lithography and Etching

Once sputtered, the wafers were ready to be processed inside the NSL. Before the sputtered wafers were brought into the NSL for processing, we drew the ion trap design in a CAD program, Layout Editor[4].

To begin the processing, we cleaned the wafer surface with a solvent wash which is an acetone rinse followed by methanol and then isopropyl alcohol. After cleaning the wafer surface, we spun PR1-2000A photo-resist, purchased from Futurrex, Inc.[5], at 5000 rpm for sixty seconds. Next, we baked the wafer on a hot-plate at 90°C for three minutes before we exposed the CAD pattern in a µPG 101 tabletop laser pattern generator made by Heidelberg Instruments[6]. We set the instrument to a single speed exposure with 50% laser power at 10 mW.

We developed the pattern with undiluted Futurrex resist developer (RD-6) for 70 seconds. We then inspected the wafers under an optical microscope to make sure all the features developed properly. An example of a fully developed wafer is shown in Figure 5-1. This photo-resist layer is used as an etch mask during the carbon tetrafluoride - oxygen (CF_4/O_2) etching process performed in a Plasma-Therm[7] 790 series reactive ion etcher (RIE).

Before we began etching, we removed contaminants from the chamber using the preconfigured "NEW CLEAN" process which cleaned for 5 minutes with the same mixture of carbon tetrafluoride (CF_4) and oxygen (O_2) that we used for the etch. We then placed the wafer onto the conductive center of the chamber and pumped down until the pressure stabalized below 8×10^{-5} Torr for ten seconds. In order to prepare the chamber for the etch, we flowed 15 scmm of CF_4 and 1.5 sccm of O_2 into the chamber. We also flowed 7.5 sccm of helium to form the plasma and waited until

[4]http://www.layouteditor.net/
[5]http://futurrex.com/en/
[6]http://www.himt.de/en/home/
[7]http://www.plasmatherm.com/

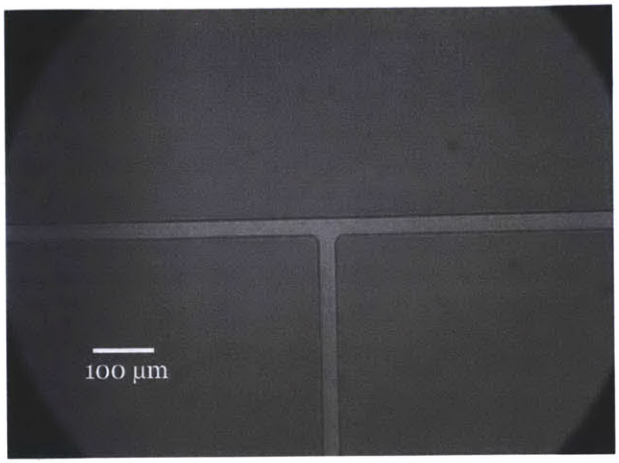

Figure 5-1: Giants5 as seen after it was developed but before etching. This chip was fabricated with NR9-3000P a negative tone resist and was developed in RD6. The dark gray region is the resist while the light region is bare Nb. Image taken by Adam McCaughan.

the total pressure in the chamber stabilized at 20 mTorr. We used a RF plasma with a power of 150 W and etched for 30 minutes.

Next, we inspected the chip to look for residual layers of Nb inside the trenches between the electrodes using a camera on the DekTak profilometer. If any Nb remained we would etch for an additional four minutes. After the etch we stripped the resist by sonicating the chip in acetone for five minutes, then rinsed the chip in a solvent wash. Figure 5-2 shows what the chip looks like after being etched and stripped of photo-resist using the same microscope used before the etch instead of the DekTak camera.

After fabricating the trap, we wirebonded it to a printed circuit board (PCB) in order to make electrical connections to the trap with standard electrical components. We designed the PCB using the same Layout Editor program that we used to design the traps, then sent the files to Advanced Circuits[8] for production on Rogers 4350 dielectric. We use a Westbond[9] model number 7476D manual wirebonder with TCSOE-1/16-750-45-GW-1630-M 0.001 inch diameter aluminum wire.

[8]http://www.4pcb.com/
[9]http://www.westbond.com/

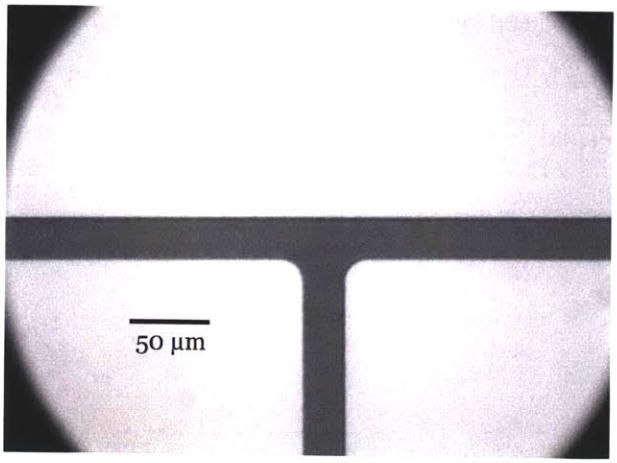

Figure 5-2: Giants5 as seen after it was etched. The light region is the reflective Nb layer and the dark region is the sapphire. Image taken by Adam McCaughan.

5.2 Experimental Apparatus

Similar to the fabrication process, we had complete control of the experimental apparatus to ensure that the traps were cooled below the superconducting transition temperature and to reduce spurious heating sources for the trapped ions. In our experiment we use lasers and an optic imaging network which are integrated into the cryostat to generate, cool and image the ions. We also use a microwave source and amplifier to provide the experiment with the necessary signals for driving rotational transitions of polar molecular ions.

5.2.1 Closed-Cycle Cryostat

We mounted the wirebonded trap into a closed-cycle, vibrationally-damped cryostat Model DE-210 from ARS Cryogenics[10] integrated with an ARS-M600 water-cooled helium compressor. The cryostat operates under ultra-high vacuum and the vacuum shield has feed-throughs and windows for electrical and optical access on a spherical octagon purchased from Kimball Physics[11].

The vibration damping in the cryostat raises the temperature of the center stage

[10]http://www.arscryo.com/index.html
[11]http://www.kimballphysics.com/

slightly so that the base temperature is 5.5 K. The vibration damping also reduces the cooling power, which is the maximum heat load that can be tolerated before the temperature is increased. The cold stage has a cooling power of < 1 W at 5.5 K. Surrounding the 5.5 K stage is a 40 K stage that reduces the radiative heating from the hot vacuum shield. This 40 K stage has approximately 10 W of cooling power.

Thermal Isolation

Since the stages of the cryostat can only tolerate a specific load, we took several steps to make sure that we minimized the thermal energy that could be delivered by the electrical connections. The design changes discussed in this section were made to ensure that the traps could maintain superconductivity when we ran the experiment.

The amount of heating power delivered through conduction from a hot body to a cold body is dependent on the material and geometry of the connection as well as on the temperature difference of the two sides. The equation is

$$P = \sigma_{\mathrm{T}} \frac{A\Delta T}{L} \tag{5.1}$$

where σ_{T} is the thermal conductivity in $\mathrm{Wm^{-1}K^{-1}}$, A is the cross-sectional area of the connection, L is the length of the material and ΔT is the temperature difference in kelvin. The thermal load from an electrical connection is reduced by changing to a material with less thermal conductivity. The thermal load can also be reduced by changing the geometry of the wire, either by reducing the cross-sectional area or by making the wire longer.

We applied this idea of thermal isolation to reduce the thermal load on the cryostat from the RF and microwave lines. The original RF wire was a 5 inch long 18 AWG solid copper wire which went straight from the room-temperature feed-through to the 5.5 K stage and delivered 0.7 W of heating power. We replaced the original RF wire with a nickel-chrome alloy wire of a similar gauge and length, but because the thermal conductivity of nickel-chrome is smaller, the heat load was only 0.02 W. We also use isolating microwave cables to run between the room temperature vacuum

chamber and the 5.5 K stage. These cables were made of stainless-steel and only deliver 0.1 W of heating power each. The microwave cables were 0.086 inch diameter semi-rigid stainless-steel microwave cables from Micro-Stock[12], part number UT-85-SS. Making the RF and microwave connections with isolating materials helped reduce the temperature of the cryostat. We made these changes in between the Giants traps and the Cubs/White Sox traps.

Thermal Sinking

Thermal isolation will reduce the loading of a connection from a high-temperature environment into a low temperature environment but once inside the cold environment everything must be at the same temperature to avoid localized heating. The ion trap is the most important part of the experiment to keep cold therefore, we performed a complete redesign of the mounting hardware to ensure that the trap was superconducting. This section describes the changes made to the cryostat to ensure proper thermal connections.

The 5.5 K stage cools the trap through thermal conductance. The original design of the inner chamber did not provide proper thermal connections so the Nb could not be cooled below the superconducting transition temperature. The original mount had two pin-grid-arrays and a PCB placed between the ion trap and the cold stage, as shown in Figure 5-3. The pin-grid-arrays are mostly teflon, while the PCB material is a fiberglass that is not thermally conductive. This mount for the ion traps almost completely isolated the trap from the cold temperatures of the baseplate.

Because of the problems with the thermal conductivity, we designed a new mount that allowed the trap to have direct thermal contact with the 5.5 K chamber. The design required a new PCB that had a hole in the center to allow the chip to be placed directly on the copper below. This PCB sat on a two part copper frame that was bolted to the 5.5 K stage. The lower part of the frame remains inside the cryostat at all times, while the top piece is taken out when the traps are changed. This stack is shown in Figure 5-4.

[12]http://www.microstock-inc.com/

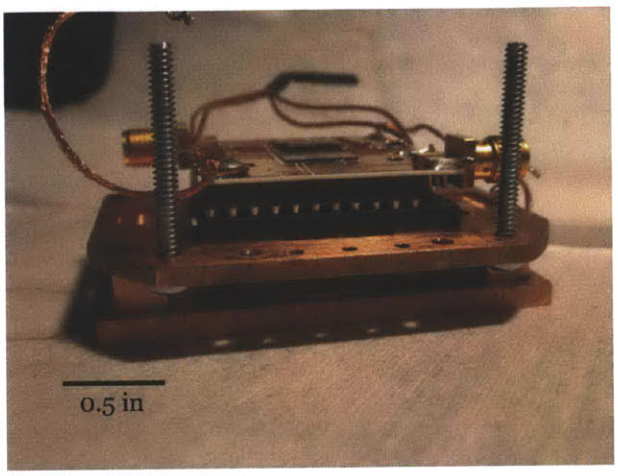

Figure 5-3: The original mounting of the chip was a stack of machined copper parts with two PGA boards and the chip would sit on the Roger's substrate. The extra copper braid on the left was used to provide some thermal sinking to the top layer of the PCB.

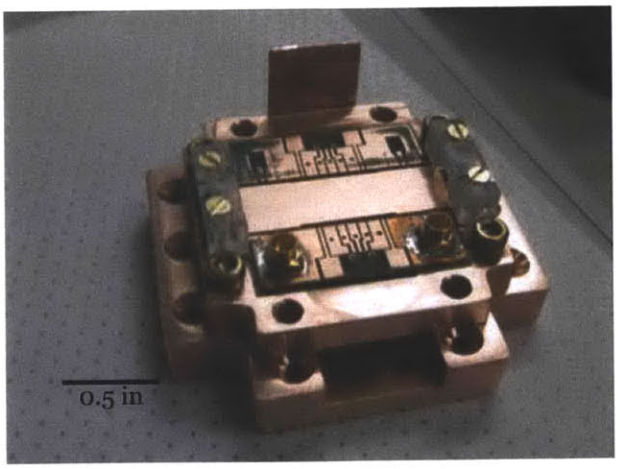

Figure 5-4: Redesigned chip holder for performing our experiment. The additional thermal conductivity to the cold stage made it possible to lower the temperatures of the chips below the superconducting critical temperature.

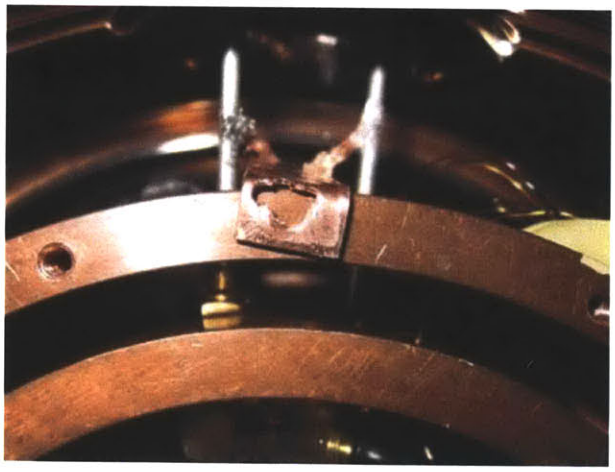

Figure 5-5: Thermal sinking of microwave line to the 40 K shield. This was also done at the 4 K stage.

Another change we made from the old design was to use brass screws. We chose brass screws because brass contracts more than copper at low temperatures, tightening the copper pieces together. We also used brass screws to tighten a plastic frame that pressed the traps into a piece of soft indium foil in order to ensure good thermal contact between the sapphire and the copper.

The electrical connections in our chamber were thermally sunk to the 5.5 K stage before being connected to the PCB to avoid a potential for localized heating near the ion traps. Both of the isolating systems discussed in the last section were connected to a second material inside the 5.5 K cold stage that had high thermal contact to the 5.5 K stage. The RF wires were wrapped around a copper post five times before making a connection to the PCB. The isolating microwave cables terminated in bulk-head connectors and a set of copper semi-rigid microwave cables were used to connect from the bulk-head connectors to the PCB. This copper cable was also soldered to a short run of copper mesh that was bolted to the 5.5 K stage. This caused the 5.5 K stage to increase in temperature so we made another another thermal connection between the middle of the insulating cable to the 40 K shield. This extra connection provided an alternate path for the heat load and shown in Figure 5-5.

5.2.2 Ion Sources and Imaging

In addition to electrical access our cryostat has optical access that allowed our group to use lasers to generate, cool and image our ions. Additionally, the optics inside the cryostat were integrated into the cold stages to avoid local heat sources near the ions.

We used laser ablation to generate ions near the trap. Since we needed to be able to use both strontium and strontium chloride for our experiment, we used laser ablation. Laser ablation is a process that creates a lot of contaminants and unwanted particles[13], but it is useful for loading mixed species traps efficiently. We used both strontium titanate ($SrTiO_3$) crystals from MTI Crystals and pressed strontium chloride ($SrCl_2$) pellets as ion sources for the experiment. We used the $SrTiO_3$ target to load Sr^+ ions without the $SrCl^+$ molecular ions so that the traps could be optimized because this ablation process was cleaner than ablation from the $SrCl_2$ pellet. For ablation, we used a high power neodymium-doped yttrium aluminum garnet, Nd:YAG, pulsed laser with about 8 mJ of energy per pulse with a pulse length of 5 ns.

As discussed in Chapter 2 we needed two lasers to cool the Sr^+ ions inside the trap in addition to the ablation laser that generated the ions. Both of these lasers are stabalized laser diodes with one operating at 422 nm and the other at 1091 nm. Also, as discussed in Chapter 2, a side effect of using these lasers to cool the ions is that the fluorescence signature can be used to detect the ions. We used an Andor[13] iXon3 camera to image the ions. We also use a photo-multiplier-tube (PMT) to quantify the fluorescence signal from the ions. A full diagram of the cryostat system with these optics is shown in Figure 5-6.

5.2.3 Microwave Network

After loading SrCl+ into the trap, we needed to bring in high-powered microwave signals to drive the rotational transitions. We used an Agilent[14] N5183 analog microwave signal generator followed by a QPJ-06183630-A0 microwave amplifier from

[13]http://www.andor.com/
[14]http://www.agilent.com/

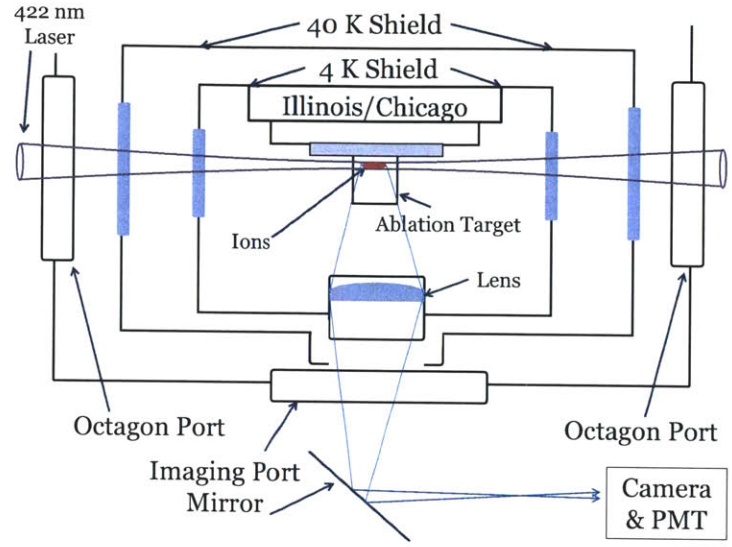

(a)

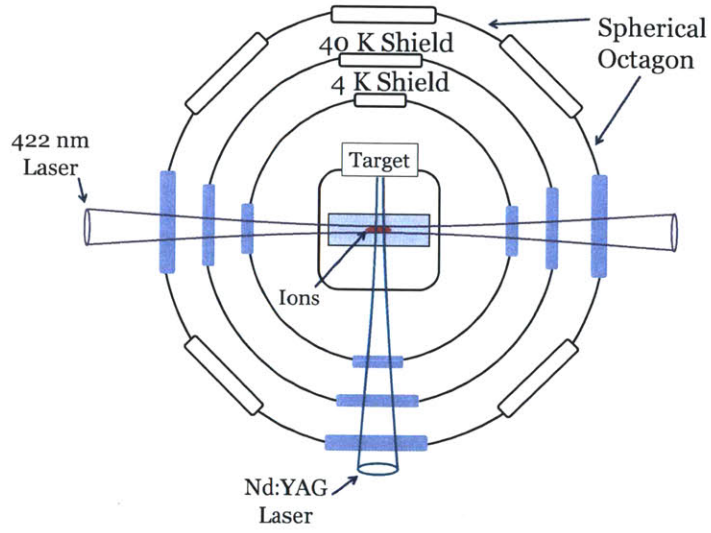

(b)

Figure 5-6: Side view of the cryostat system (a) and a front view of the cryostat (b). For clarity, none of the electrical connections are included.

Quinstar[15] to amplify the microwave signals. In series with the amplifier we used a Raditek[16] RADI-2-18-P-S3-1WR-02 peripheral mode wide band isolator that works from 2 to 18 GHz. This isolator ensured that no microwave power was reflected into the microwave amplifier. All of the cabling that connected the microwave network outside of the cryostat was SS402 low-loss microwave cable from Crystek[17]. The total gain of this microwave amplifier network at 6.5 GHz is $\sim$ 27 dB, as measured with a Minicircuits[18] ZX47-40-S+ power meter.

[15]http://www.quinstar.com/
[16]http://raditek.com/
[17]http://www.crystek.com/microwave/
[18]http://www.minicircuits.com/

Chapter 6

Experimental Results

Once we fabricated the chips and cooled down the cryostat we were ready to test the traps. This chapter discusses the different designs that we tested in this project, most of which were designed by Paul Antohi[2].

The Dodgers design was the first attempt to trap ions using a niobium ion trap fabricated with the process described in Chapter 5. The Dodgers traps had dielectric charging issues as well as problems with arcing from the RF electrodes to the rest of the trap. The Giants design incorporated changes to combat the problems with the Dodgers traps and was the first trap to successfully trap Sr^+ ions. However, these traps were not superconducting. Therefore, we had to change the design of the cryostat chamber to ensure superconductivity of the traps before we could perform our experiment to heat the Sr^+ cloud by driving rotational transitions in $SrCl^+$. We used the Cubs traps to verify that the chamber could maintain superconductivity of the traps while bearing the full heat load of the experiment. Cubs traps did not have the integrated CPW transmission line, therefore we fabricated the White Sox traps that did have an integrated CPW line. We then used these traps to perform our target experiment by sending in high power microwaves in an attempt to drive rotational transitions of $SrCl^+$ and look for Sr^+ cloud heating. The results of these tests have not shown the expected heating as of this writing. Therefore, at the end of the chapter I outline the steps we plan to take in the future in order to ensure the project succeeds.

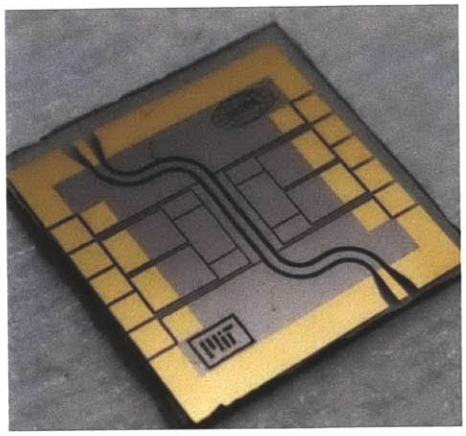

Figure 6-1: Dodgers1 trap tested in June 2010. Could not trap ions because of charging problems.

6.1 Dodgers Traps

The Dodgers series was the first series of traps that we tested in the cryostat. The results of the tests with the Dodgers traps showed that there were two problems with our first designs. The first problem, on Dodgers1, was that the exposed dielectric caused charging that altered the stability of the trapping potential. Dodgers2 and Dodgers3 incorporated our attempt to reduce the dielectric area, but this change resulted in arcing and catastrophic failure.

The first Dodgers trap was designed with large gaps between the RF electrodes and the center conductor in order to impedance match the CPW waveguide to the $50\,\Omega$ impedance. This exposed dielectric caused distortions to the trapping potential that prevented the ions from staying trapped. Dodgers1 is shown in Figure 6-1. This design was made with an old fabrication technique that included evaporated gold pads for connecting the trap to the PCB.

Two more Dodgers chips were made with narrow gaps of $10\,\mu m$ and $15\,\mu m$ to counteract the dielectric charging issues. The high-voltage RF signals arced across these narrow gaps and destroyed the DC pads as shown in Figure 6-2.

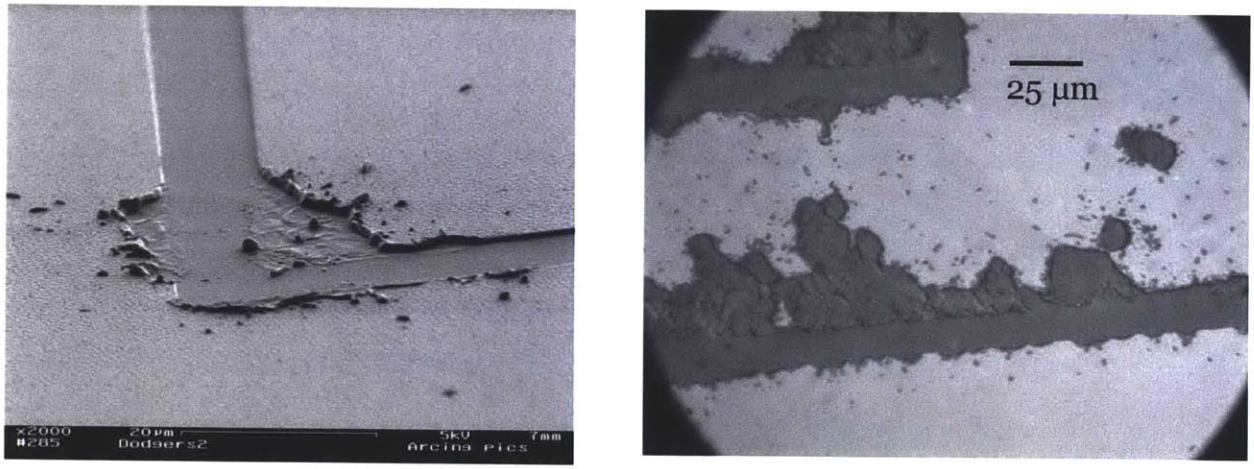

Figure 6-2: The SEM of the remains of Dodgers2 (left) and an optical micrograph of the damage to Dodgers3 (right) caused by arcing from the RF electrode.

6.2 Giants Traps

The Giants series was the second series of traps that we tested. We solved the arcing problem by rounding the corners of the electrodes to reduce the local field intensities. The Giants traps also had a larger trap depth than the Dodgers traps and so we expected them to trap ions more efficiently. An image of Giants7 is shown in Figure 6-3.

Giants1 had 25 µm gaps while Giants2 had 15 µm gaps, but neither traps actually worked. Giants3 and Giants4 were designed but were never tested inside the cryostat. Giants5 had 15 µm gaps and was the first of our traps to hold ions in a stable trap. We also produced Coulomb crystals as shown in Figure 6-4. This trap failed after a relatively short time in the cryostat because of build up of contaminants from the ablation process

Giants5's success in trapping ions encouraged us to keep the same electrode geometry, but the short life span of the trap forced us to increase the gaps in Giants7. We increased the gaps to 25 µm to reduce the possibility of contaminants shorting across two electrodes. There were more than six different Giants7 designs that were labeled as A-F and the same electrode geometry was repeated in both the Cubs and White Sox traps.

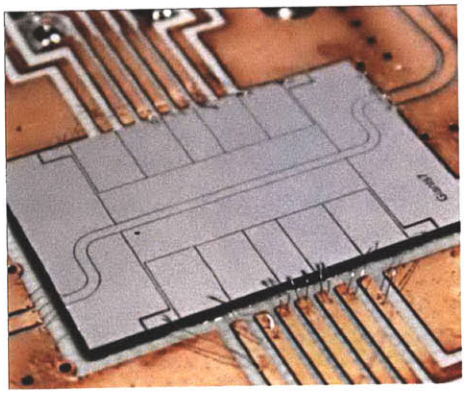

Figure 6-3: This Giants7 trap was tested in August 2010. We rounded the corners of the pads reducing the arcing problem. The gaps in this trap were all 25 µm. The PCB that it is mounted on was changed so that the PCB electrodes matched those on the trap.

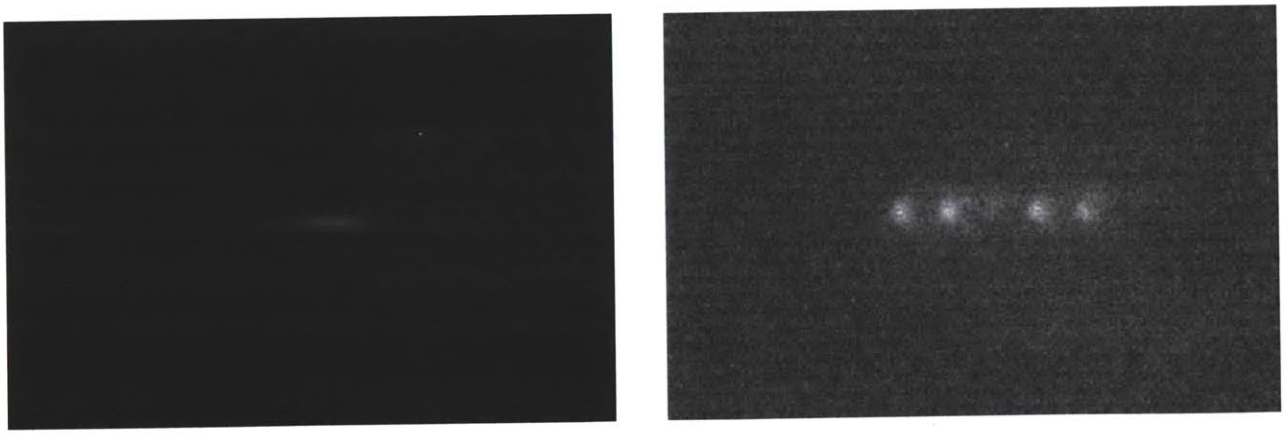

Figure 6-4: Images of trapped ions above Giants5 in a cloud state (left) and a crystallized state (right). The non-fluorescing ion is not Sr^{88}, though mass spectroscopy was not performed to verify the species.

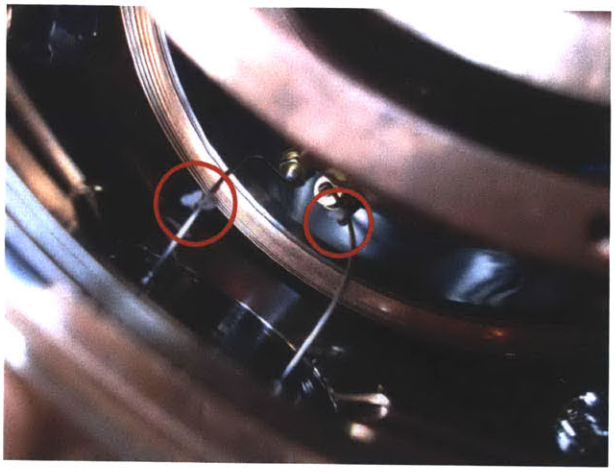

Figure 6-5: The original microwave cables from Microstock that failed when high power signals were used inside the cryostat.

When we applied microwaves to the Giants7 traps we found that the original cabling of 0.034 inch diameter stainless-steel coaxial cables could not withstand the high power signals from the amplifier. These cables cracked and the insulating dielectric melted out of the cables as shown in Figure 6-5. We replaced the microwave network with RG316DS-P cables from Crystek Microwave, but this connection from the room temperature feed-through in the vacuum shield to the 5.5 K stage raised the temperature to more than 30 K.

A large experimental redesign began in September 2010 because of the problems with the microwave network and the poor thermal sinking discussing in Chapter 5. We redesigned and built a new cabling network and thermally engineered the cryostat to achieve lower temperatures. This process concluded in February of 2011 and we began testing the Cubs and White Sox series.

6.3 Cubs and White Sox Traps

After the redesign to reduce the temperature inside the cryostat we built the third and fourth round of traps. These new traps, the Cubs and White Sox traps, fit the geometry of the new mounting hardware. We tried our experiment several times but have failed to see expected heating of the Sr^+ ion cloud.

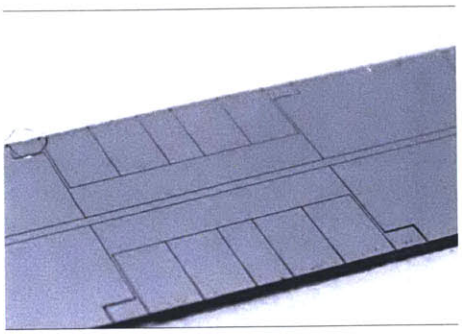

Figure 6-6: White Sox1A used the same electrodes from Giants but the transmission line and chip length were altered to fit inside the new mounting hardware in the cryostat.

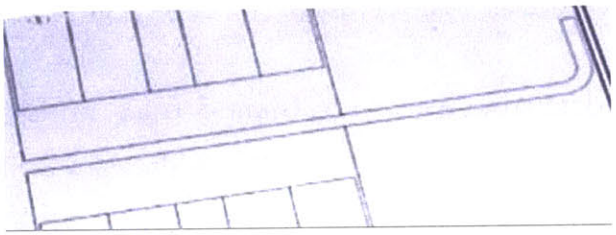

Figure 6-7: Stub resonator on Cubs1 that was used to test for superconductivity. The hook on the right is used to increase the coupling capacitance to the resonator.

The electrodes for both White Sox and Cubs traps were the same, but Cubs traps were used for in situ testing of the superconductivity of the niobium layers during the ion trapping process. The WhiteSox design was tested through May 2011 using high power microwave signals to drive the rotational transition in $SrCl^+$. We have performed the most thorough search for heating in the Sr+ cloud with the White Sox traps. White Sox1A is shown in Figure 6-6.

We built the Cubs traps to test for superconductivity while the ion trap was running. Cubs1 had a transmission line stub resonator with a large coupling capacitance to a feed-line as shown in Figure 6-7. If the trap was superconducting, we would expect the resonator to have a high quality factor.

However, we did not see a resonance in Cubs1. We therefore incorporated a long, meandered wire as a second in situ test for superconductivity of the trap. This wire was 50 µm wide and almost 0.5 m long and it had a high resistance in the normal state but almost zero-resistance when superconducting. We measured the resistance

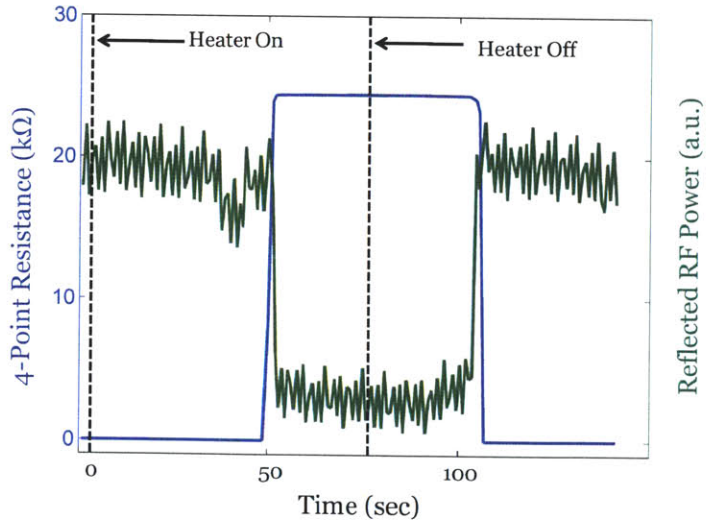

Figure 6-8: Proof of superconductivity with two different signals, the 4-point DC resistance measured across a meandered 1 m long wire (blue) and the reflected RF power from the electrodes (green).

with a 4-point technique to eliminate the resistance of the wires leading up to the trap. Figure 6-8 shows a time scan of the resistance across the meandered wire as the temperature inside the cryostat was increased by applying current to a heater. The power reflected from the RF electrodes is also plotted in Figure 6-8. This RF reflection test can be performed using any ion trap which makes it a useful test for superconductivity even without the meandered wire.

6.4 Heating Signature

Once we could consistently achieve superconductivity inside the cryostat we began testing the White Sox traps as the White Sox traps were built to for high power microwave signals. We tested these traps until they became contaminated from the ablation process, making trapping impossible.

We attempted to drive the rotational transitions in $SrCl^+$ in White Sox1B where the maximum microwave power we could apply was $\sim 35\,\mathrm{mW}$ before the chip would switch to the normal state. We set the power under the $\sim 35\,\mathrm{mW}$ limit and then performed a frequency sweep around 6.5 GHz which is the expected frequency of the

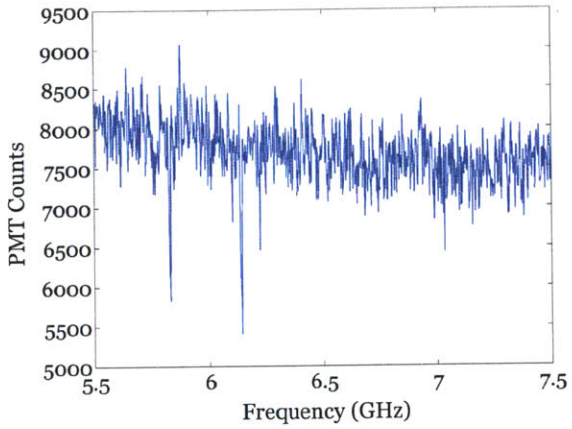

Figure 6-9: The first microwave scan in White Sox1B performed at 16 mW of microwave power into the transmission line.

rotational transition. During the frequency sweep we monitored the fluorescence in our Hamamatsu photo-multiplier-tube (PMT) which measured the number of counts per second from the ion cloud. The results of this first sweep are shown in Figure 6-9.

We performed the first scan after ablation loading from the $SrCl_2$ pellet which our group has shown loads both Sr^+ and $SrCl^+$ ion species[13]. However, we wanted to verify the presence of both ion species so we performed mass spectroscopy on the trapped ion clouds. We loaded once from the $SrTiO_3$ target and performed a mass spectroscopy scan which gave us a signature for the secular frequency of Sr^+. The scan of Sr+ ions only is in Figure 6-10(a). Then we performed a scan after loading from the $SrCl_2$ target to look for the $SrCl^+$. The scan shown in 6-10(b) was taken with 10 times larger tickle amplitude than the scan in Figure 6-10(a). We need a high amplitude in order to see the effect of the $SrCl^+$ resonance on the Sr^+ fluorescence because the reduction in fluorescence is a second order effect. The scan shown in Figure 6-10(b) does not conclusively show the presence of $SrCl^+$.

Even though the mass spectroscopy scans were inconclusive we attempted one more time to excite the rotational transition in $SrCl^+$. The result was no different than the first attempt and this microwave scan is shown in Figure 6-11.

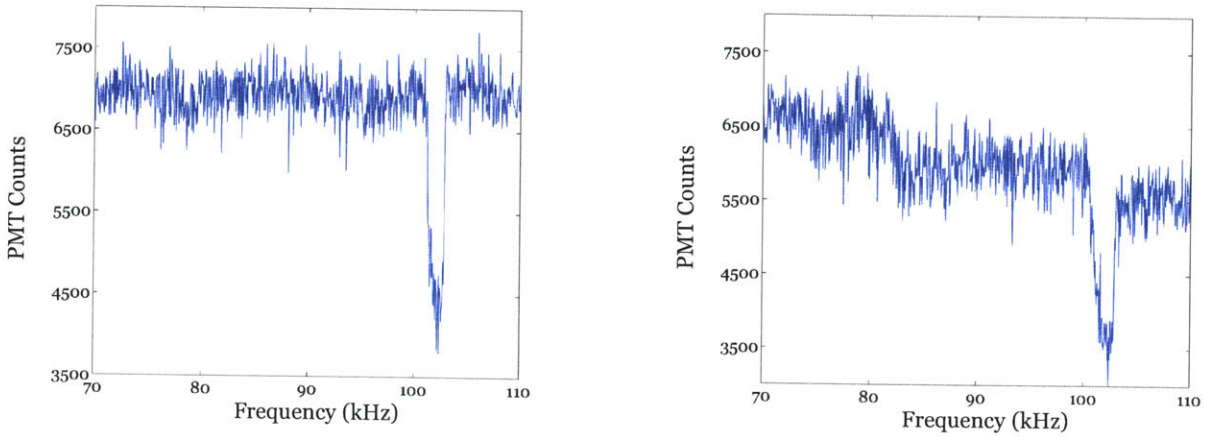

Figure 6-10: Mass spectroscopy scan with of White Sox1B to verify the presence of ion species in the trap. The dip at 85 kHz in (b) might be from exciting $SrCl^+$ out of the ion traps.

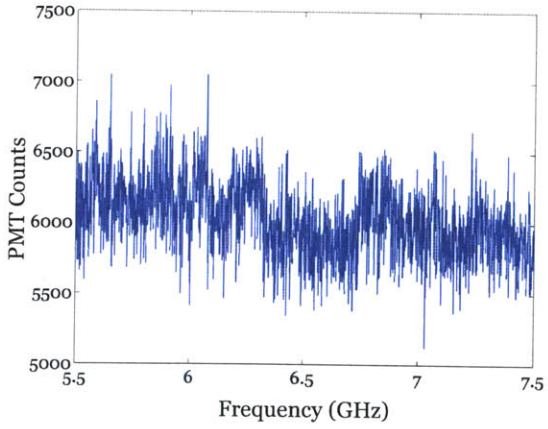

Figure 6-11: The second microwave scan in White Sox1B performed at 28 mW of microwave power into the transmission line.

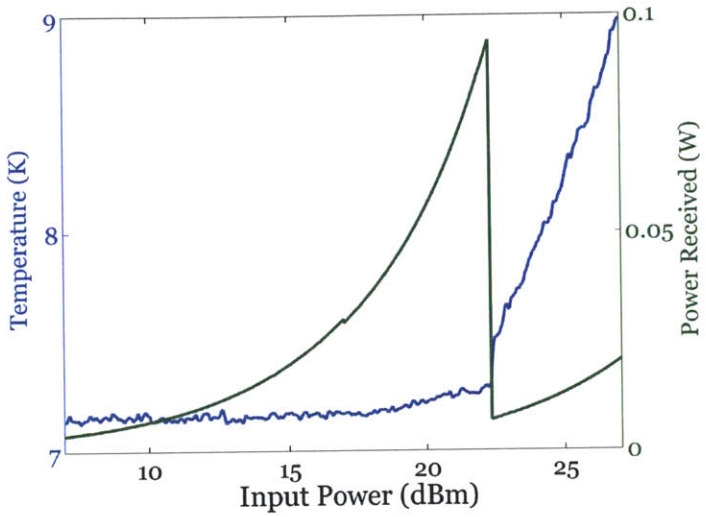

Figure 6-12: Power transmitted through the cryostat (green) until the superconducting transition occurs near 0.1 W, the temperature is plotted for the same input powers (blue). The frequency was fixed at 6.5 GHz.

6.5 Future Plans

After failing to see the predicted heating we began investigating further changes to the experimental setup to improve the conditions of the experiment. Preliminary data suggests that the microwave power can be increased by a factor of three, while further improvements are possible. We are also investigating the expected heating of a Coulomb crystal composed of both Sr^+ and $SrCl^+$ when we drive the rotational transition of $SrCl^+$.

The maximum microwave power we could apply to White Sox1B was 15 dBm, or $\sim$ 32 mW, before the chip would transition to the normal state. We believed that the transition occurred because of localized heating caused by the wirebonds. We tested this hypothesis by using nine wirebonds on the center electrode in White Sox 1C. The additional wirebonds reduce the current through each bond and therefore reduce the heating. The maximum power increased to almost 100 mW in White Sox 1C as shown in Figure 6-12. With 0.1 W of input power the electric field at the ion is approximately $500\,\mathrm{V m^{-1}}$.

Based on the superconducting transition illustrated in Figure 6-12, we realized the

niobium could be transitioning to the normal state because of loss in the transmission line. We plan to test if our niobium layer is the limiting factor by increasing the thickness of the Nb layer for the trap from 200 nm to 400 nm. If this modification allows the trap to support higher microwave power, then we may be able to more quickly drive transitions in $SrCl^+$.

We are also investigating using a low-Q resonator inside the cryostat to amplify the electric field near the ions. We would like to use a low-Q resonator to still have some range in the microwave scan around the expected rotational transition frequency. There has been recent work in constructing high-Q capacitively coupled resonators with a DC bias applied to this resonator[4] and we are working to expand this work with low-Q resonators of a similar type.

Lastly, we are investigating the possibility of crystallizing the ion cloud and performing the experiment in the crystallized state. The advantage of the crystal state is that the fluorescence signal is much higher which makes the experiment is more sensitive. The problem with the crystal state, however, is that the reduction in collisions also makes the interaction between the atomic ion and polar molecular ion weaker.

Appendix A

Chips

This is a more complete list of all traps designed and tested in Table A.1. This list includes traps that were not discussed in the main text of the thesis.

Table A.1: Complete list White Sox and Cubs series of ion traps brief comments about the results

Trap Series	Chip Name	Design Date	Comments
Yankees	Yankee1	June 2010	Never constructed, the goal was to use Sonnet to map out the parameter space of line length and gap size for constructing high-Q resonators
	Yankee2	June 2010	Simulated in Sonnet
	Yankee3	June 2010	Simulated in Sonnet
	Yankee4	June 2010	Simulated in Sonnet
	Yankee5	June 2010	Simulated in Sonnet
	Yankee6	June 2010	Simulated in Sonnet
	Yankee7	June 2010	Simulated in Sonnet
	Yankee8	June 2010	Simulated in Sonnet

Continued on Next Page...

Table A.1 – Continued

Trap Series	Chip Name	Design Date	Comments
	Yankee9	June 2010	Simulated in Sonnet
Dodgers	Dodgers1	June 2010	Ion trap never worked, arcing problems
	Dodgers2	July 2010	Changed design from Dodgers 1, 10 μm gaps caused arcing problems
	Dodgers3	July 2010	Same design as Dodgers2 but with 15μm gaps, still arcing problems
Giants	Giants1	July 2010	arcing problems
	Giants2	August 2010	Larger trap depth than Dodgers design, corners of the electrodes were rounded to prevent arcing. This chip did not trap ions
	Giants3	August 2010	Added a resonator to Giants2 and simulated but it was never constructed
	Giants4	August 2010	Like Giants 3 this chip was never consructed and contained a resonator
	Giants5	August 2010	Increased the gaps around the electrodes to 25 μm to reduce shorting problems and this was the first ion trap to work
	Giants6	August 2010	This chip also had a resonator like Giants3 and Giants4 and the resonator was constructed and tested in an immersion apparatus

Continued on Next Page...

Table A.1 – Continued

Trap Series	Chip Name	Design Date	Comments
	Giants7A-F	August 2010	This trap was tested mulitple times and led to our understanding that the ion traps were not superconducting. After the thermal redesign that changed to Chicago/Illinois mounting hardware the trap geometry was used again in the White Sox and Cubs series. Same design was used after one chip would become contaminated
White Sox	White Sox1A	February 2011	This chip was used to verify superconductivity while trapping but the thermal load was still too high. The chip did trap but the transmission line was not operating correctly
	White Sox1B-E	March 2011	After the Cubs series verified the superconductivity a second White Sox1 was made to try putting in high power microwaves. The chips were changed out after becoming contaminated from the $SrCl_2$ target
Cubs	Cubs1	February 2011	The same trap design as White Sox and Giants but a stub resonator was used in order to test for superconductivity
	Cubs2	March 2011	A four point measurement line was included into the trap to verify superconductivity separately from the microwave measurements

Appendix B

Matlab Code

B.1 Isosurface Trapping Potential

```
function TrappingPotentialIsoSurface
%  Using the models from M.G. House "Analytic Model for Electrostatic
%  Fields in Surface-Electrode Ion Traps" 2008, Phys Rev A, Vol 78, Issue 3
%  I have calculated the trapping potential and the secular frequencies for
%  Giants8 with 1000 Vpp amplitude on the RF lines
%
%  This method assumes that the gaps are small compared to the size of the
%  electrodes and can largely be ignored.

%Set the Applied Voltages
Vquad = 0;
Vmid = -30;
Vend = 21;
Vrf = 500;


% Initialize geometry coefficients for Giants7/Cubs/WhiteSox
G = 25;
```

```
A = 400;
B = 1780;
w1 = 1300;
w2 = 1850;
w3 = 1850;

%Initialize the ion being used (scales pseudo potential)
% Strontium numbers Z = 1, m = 1.46*10^-25kg, Vrf = 300V, Omega = 2pi*50MHz
Zn = 1;
e = 1.6022*10^-19;
m = 1.46*10^-25;
Omega = 2*pi*6.01*10^6;
prefact = Vrf^2*Zn^2*e^2/(4*m*Omega^2);

% Set volume over which to calculate the potential
Dx = 10;
Dy = 50;
Dz = 10;
x = -400:Dx:400;
dx = Dx*10^-6;
z = 400:Dz:800;
dz = Dz*10^-6;
y = -2000:Dy:2000;
dy = Dy*10^-6;
[X,Y,Z] = meshgrid(x,y,z);
hold on;

% Calculates the RF potential everywhere. The the 16 terms below are a
% combination of four electrode terms. I only supply the upper right
% quadrant locations and then I calculated the field after making some
```

```
% symmetry arguments that the upper right can be copied into the other four
% quadrants. The terms do not look prettier but it allows for fewer inputs
% for each electrode
x1 = A/2+G/2;
x2 = x1+B+G/2;
y1 = 0;
y2 = w1/2+w2+w3+3*G;
phi_elec = 1/2/pi*...
    (atan((x2-X).*(y2-Y)./(Z.*sqrt(Z.^2+(x2-X).^2+(y2-Y).^2)))-...
    atan((x1-X).*(y2-Y)./(Z.*sqrt(Z.^2+(x1-X).^2+(y2-Y).^2)))-...
    atan((x2-X).*(y1-Y)./(Z.*sqrt(Z.^2+(x2-X).^2+(y1-Y).^2)))+...
    atan((x1-X).*(y1-Y)./(Z.*sqrt(Z.^2+(x1-X).^2+(y1-Y).^2)))-...
    atan((-x2-X).*(y2-Y)./(Z.*sqrt(Z.^2+(-x2-X).^2+(y2-Y).^2)))+...
    atan((-x1-X).*(y2-Y)./(Z.*sqrt(Z.^2+(-x1-X).^2+(y2-Y).^2)))+...
    atan((-x2-X).*(y1-Y)./(Z.*sqrt(Z.^2+(-x2-X).^2+(y1-Y).^2)))-...
    atan((-x1-X).*(y1-Y)./(Z.*sqrt(Z.^2+(-x1-X).^2+(y1-Y).^2)))-...
    atan((x2-X).*(-y2-Y)./(Z.*sqrt(Z.^2+(x2-X).^2+(-y2-Y).^2)))+...
    atan((x1-X).*(-y2-Y)./(Z.*sqrt(Z.^2+(x1-X).^2+(-y2-Y).^2)))+...
    atan((x2-X).*(-y1-Y)./(Z.*sqrt(Z.^2+(x2-X).^2+(-y1-Y).^2)))-...
    atan((x1-X).*(-y1-Y)./(Z.*sqrt(Z.^2+(x1-X).^2+(-y1-Y).^2)))+...
    atan((-x2-X).*(-y2-Y)./(Z.*sqrt(Z.^2+(-x2-X).^2+(-y2-Y).^2)))-...
    atan((-x1-X).*(-y2-Y)./(Z.*sqrt(Z.^2+(-x1-X).^2+(-y2-Y).^2)))-...
    atan((-x2-X).*(-y1-Y)./(Z.*sqrt(Z.^2+(-x2-X).^2+(-y1-Y).^2)))+...
    atan((-x1-X).*(-y1-Y)./(Z.*sqrt(Z.^2+(-x1-X).^2+(-y1-Y).^2))));
x1 = A/2+G;
x2 = x1+B;
fill3([x1 x2 x2 x1],[y2 y2 -y2 -y2],[0 0 0 0],'g')
fill3(-[x1 x2 x2 x1],[y2 y2 -y2 -y2],[0 0 0 0],'g')

% This calculates the influence of the last part of the RF wire that runs
```

```
% on the outside of the DC pads.
x1 = A/2+G;
x2 = 5000;
y1 = w1/2+G+w2+G+w3+G;
y2 = y1+80;
rf_end = 1/2/pi*...
    (atan((x2-X).*(y2-Y)./(Z.*sqrt(Z.^2+(x2-X).^2+(y2-Y).^2)))-...
    atan((x1-X).*(y2-Y)./(Z.*sqrt(Z.^2+(x1-X).^2+(y2-Y).^2)))-...
    atan((x2-X).*(y1-Y)./(Z.*sqrt(Z.^2+(x2-X).^2+(y1-Y).^2)))+...
    atan((x1-X).*(y1-Y)./(Z.*sqrt(Z.^2+(x1-X).^2+(y1-Y).^2)))-...
    atan((-x2-X).*(y2-Y)./(Z.*sqrt(Z.^2+(-x2-X).^2+(y2-Y).^2)))+...
    atan((-x1-X).*(y2-Y)./(Z.*sqrt(Z.^2+(-x1-X).^2+(y2-Y).^2)))+...
    atan((-x2-X).*(y1-Y)./(Z.*sqrt(Z.^2+(-x2-X).^2+(y1-Y).^2)))-...
    atan((-x1-X).*(y1-Y)./(Z.*sqrt(Z.^2+(-x1-X).^2+(y1-Y).^2)))-...
    atan((x2-X).*(-y2-Y)./(Z.*sqrt(Z.^2+(x2-X).^2+(-y2-Y).^2)))+...
    atan((x1-X).*(-y2-Y)./(Z.*sqrt(Z.^2+(x1-X).^2+(-y2-Y).^2)))+...
    atan((x2-X).*(-y1-Y)./(Z.*sqrt(Z.^2+(x2-X).^2+(-y1-Y).^2)))-...
    atan((x1-X).*(-y1-Y)./(Z.*sqrt(Z.^2+(x1-X).^2+(-y1-Y).^2)))+...
    atan((-x2-X).*(-y2-Y)./(Z.*sqrt(Z.^2+(-x2-X).^2+(-y2-Y).^2)))-...
    atan((-x1-X).*(-y2-Y)./(Z.*sqrt(Z.^2+(-x1-X).^2+(-y2-Y).^2)))-...
    atan((-x2-X).*(-y1-Y)./(Z.*sqrt(Z.^2+(-x2-X).^2+(-y1-Y).^2)))+...
    atan((-x1-X).*(-y1-Y)./(Z.*sqrt(Z.^2+(-x1-X).^2+(-y1-Y).^2))));

fill3([x1 x2 x2 x1],[y2 y2 y1 y1],[0 0 0 0],'g')
fill3(-[x1 x2 x2 x1],[y2 y2 y1 y1],[0 0 0 0],'g')
fill3([x1 x2 x2 x1],-[y2 y2 y1 y1],[0 0 0 0],'g')
fill3(-[x1 x2 x2 x1],-[y2 y2 y1 y1],[0 0 0 0],'g')

grey = [0.01, 0.01, 0.01];
x1 = -A/2;
```

```
x2 = A/2;
fill3([x1 x2 x2 x1],[y2 y2 -y2 -y2],[0 0 0 0],grey)

%Calculate the gradient for use in the pseudopotential
phi_tot = phi_elec+rf_end;
[Fx,Fy,Fz]= gradient(phi_tot,dx,dy,dz);
psi_rf = (Fx.^2+Fy.^2+Fz.^2)*prefact;

% Calculate the DC end pads influences. The Zn*e term converts from voltage
% to potential energy similar to that of the RF potential
x1 = A/2+B+3*G/2;
x2 = 5000;
y1 = w1/2+G+w2+G/2;
y2 = y1+w3+G/2;
dc_end = Zn*e*Vend/2/pi*...
    (atan((x2-X).*(y2-Y)./(Z.*sqrt(Z.^2+(x2-X).^2+(y2-Y).^2)))-...
    atan((x1-X).*(y2-Y)./(Z.*sqrt(Z.^2+(x1-X).^2+(y2-Y).^2)))-...
    atan((x2-X).*(y1-Y)./(Z.*sqrt(Z.^2+(x2-X).^2+(y1-Y).^2)))+...
    atan((x1-X).*(y1-Y)./(Z.*sqrt(Z.^2+(x1-X).^2+(y1-Y).^2)))-...
    atan((-x2-X).*(y2-Y)./(Z.*sqrt(Z.^2+(-x2-X).^2+(y2-Y).^2)))+...
    atan((-x1-X).*(y2-Y)./(Z.*sqrt(Z.^2+(-x1-X).^2+(y2-Y).^2)))+...
    atan((-x2-X).*(y1-Y)./(Z.*sqrt(Z.^2+(-x2-X).^2+(y1-Y).^2)))-...
    atan((-x1-X).*(y1-Y)./(Z.*sqrt(Z.^2+(-x1-X).^2+(y1-Y).^2)))-...
    atan((x2-X).*(-y2-Y)./(Z.*sqrt(Z.^2+(x2-X).^2+(-y2-Y).^2)))+...
    atan((x1-X).*(-y2-Y)./(Z.*sqrt(Z.^2+(x1-X).^2+(-y2-Y).^2)))+...
    atan((x2-X).*(-y1-Y)./(Z.*sqrt(Z.^2+(x2-X).^2+(-y1-Y).^2)))-...
    atan((x1-X).*(-y1-Y)./(Z.*sqrt(Z.^2+(x1-X).^2+(-y1-Y).^2)))+...
    atan((-x2-X).*(-y2-Y)./(Z.*sqrt(Z.^2+(-x2-X).^2+(-y2-Y).^2)))-...
    atan((-x1-X).*(-y2-Y)./(Z.*sqrt(Z.^2+(-x1-X).^2+(-y2-Y).^2)))-...
    atan((-x2-X).*(-y1-Y)./(Z.*sqrt(Z.^2+(-x2-X).^2+(-y1-Y).^2)))+...
```

```
    atan((-x1-X).*(-y1-Y)./(Z.*sqrt(Z.^2+(-x1-X).^2+(-y1-Y).^2))));
y1 = y1+G/2;
y2 = y2-G/2;
xp = x1+G/2;
fill3([xp x2 x2 xp],[y2 y2 y1 y1],[0 0 0 0],grey)
fill3(-[xp x2 x2 xp],[y2 y2 y1 y1],[0 0 0 0],grey)
fill3([xp x2 x2 xp],-[y2 y2 y1 y1],[0 0 0 0],grey)
fill3(-[xp x2 x2 xp],-[y2 y2 y1 y1],[0 0 0 0],grey)

%Calculate the DC quad pad influences
y1 = w1/2+G/2;
y2 = y1+w2+G/2;
dc_quad = Zn*e*Vquad/2/pi*...
    (atan((x2-X).*(y2-Y)./(Z.*sqrt(Z.^2+(x2-X).^2+(y2-Y).^2)))-...
    atan((x1-X).*(y2-Y)./(Z.*sqrt(Z.^2+(x1-X).^2+(y2-Y).^2)))-...
    atan((x2-X).*(y1-Y)./(Z.*sqrt(Z.^2+(x2-X).^2+(y1-Y).^2)))+...
    atan((x1-X).*(y1-Y)./(Z.*sqrt(Z.^2+(x1-X).^2+(y1-Y).^2)))-...
    atan((-x2-X).*(y2-Y)./(Z.*sqrt(Z.^2+(-x2-X).^2+(y2-Y).^2)))+...
    atan((-x1-X).*(y2-Y)./(Z.*sqrt(Z.^2+(-x1-X).^2+(y2-Y).^2)))+...
    atan((-x2-X).*(y1-Y)./(Z.*sqrt(Z.^2+(-x2-X).^2+(y1-Y).^2)))-...
    atan((-x1-X).*(y1-Y)./(Z.*sqrt(Z.^2+(-x1-X).^2+(y1-Y).^2)))-...
    atan((x2-X).*(-y2-Y)./(Z.*sqrt(Z.^2+(x2-X).^2+(-y2-Y).^2)))+...
    atan((x1-X).*(-y2-Y)./(Z.*sqrt(Z.^2+(x1-X).^2+(-y2-Y).^2)))+...
    atan((x2-X).*(-y1-Y)./(Z.*sqrt(Z.^2+(x2-X).^2+(-y1-Y).^2)))-...
    atan((x1-X).*(-y1-Y)./(Z.*sqrt(Z.^2+(x1-X).^2+(-y1-Y).^2)))+...
    atan((-x2-X).*(-y2-Y)./(Z.*sqrt(Z.^2+(-x2-X).^2+(-y2-Y).^2)))-...
    atan((-x1-X).*(-y2-Y)./(Z.*sqrt(Z.^2+(-x1-X).^2+(-y2-Y).^2)))-...
    atan((-x2-X).*(-y1-Y)./(Z.*sqrt(Z.^2+(-x2-X).^2+(-y1-Y).^2)))+...
    atan((-x1-X).*(-y1-Y)./(Z.*sqrt(Z.^2+(-x1-X).^2+(-y1-Y).^2))));
y1 = y1+G/2;
```

```
y2 = y2-G/2;
fill3([xp x2 x2 xp],[y2 y2 y1 y1],[0 0 0 0],grey)
fill3(-[xp x2 x2 xp],[y2 y2 y1 y1],[0 0 0 0],grey)
fill3([xp x2 x2 xp],-[y2 y2 y1 y1],[0 0 0 0],grey)
fill3(-[xp x2 x2 xp],-[y2 y2 y1 y1],[0 0 0 0],grey)

%Calculate the DC mid pads influences
y1 = 0;
y2 = w1/2+G/2;
dc_mid = Zn*e*Vmid/2/pi*...
    (atan((x2-X).*(y2-Y)./(Z.*sqrt(Z.^2+(x2-X).^2+(y2-Y).^2)))-...
    atan((x1-X).*(y2-Y)./(Z.*sqrt(Z.^2+(x1-X).^2+(y2-Y).^2)))-...
    atan((x2-X).*(y1-Y)./(Z.*sqrt(Z.^2+(x2-X).^2+(y1-Y).^2)))+...
    atan((x1-X).*(y1-Y)./(Z.*sqrt(Z.^2+(x1-X).^2+(y1-Y).^2)))-...
    atan((-x2-X).*(y2-Y)./(Z.*sqrt(Z.^2+(-x2-X).^2+(y2-Y).^2)))+...
    atan((-x1-X).*(y2-Y)./(Z.*sqrt(Z.^2+(-x1-X).^2+(y2-Y).^2)))+...
    atan((-x2-X).*(y1-Y)./(Z.*sqrt(Z.^2+(-x2-X).^2+(y1-Y).^2)))-...
    atan((-x1-X).*(y1-Y)./(Z.*sqrt(Z.^2+(-x1-X).^2+(y1-Y).^2)))-...
    atan((x2-X).*(-y2-Y)./(Z.*sqrt(Z.^2+(x2-X).^2+(-y2-Y).^2)))+...
    atan((x1-X).*(-y2-Y)./(Z.*sqrt(Z.^2+(x1-X).^2+(-y2-Y).^2)))+...
    atan((x2-X).*(-y1-Y)./(Z.*sqrt(Z.^2+(x2-X).^2+(-y1-Y).^2)))-...
    atan((x1-X).*(-y1-Y)./(Z.*sqrt(Z.^2+(x1-X).^2+(-y1-Y).^2)))+...
    atan((-x2-X).*(-y2-Y)./(Z.*sqrt(Z.^2+(-x2-X).^2+(-y2-Y).^2)))-...
    atan((-x1-X).*(-y2-Y)./(Z.*sqrt(Z.^2+(-x1-X).^2+(-y2-Y).^2)))-...
    atan((-x2-X).*(-y1-Y)./(Z.*sqrt(Z.^2+(-x2-X).^2+(-y1-Y).^2)))+...
    atan((-x1-X).*(-y1-Y)./(Z.*sqrt(Z.^2+(-x1-X).^2+(-y1-Y).^2))));
y2 = y2-G/2;
fill3([xp x2 x2 xp],[y2 y2 -y2 -y2],[0 0 0 0],grey)
fill3(-[xp x2 x2 xp],[y2 y2 -y2 -y2],[0 0 0 0],grey)
```

```
%Calculate the total trap potential
Psi_Trap = (psi_rf+dc_mid+dc_end+dc_quad);

%Find trap minimum
psi_x0 = interp3(X,Y,Z,Psi_Trap,0,0,z);
psi_x0 = psi_x0(:);
locs = find(diff(psi_x0)>0,1);

%Plot the isosurface
set(gca,'XTickLabel',[],'YTickLabel',[],'ZTickLabel',[]);
p = patch(isosurface(X,Y,Z+1500,Psi_Trap/e,psi_x0(locs)/e+0.40));
isonormals(X,Y,Z+1500,Psi_Trap/e+0.4,p);
set(p,'facecolor','red','edgecolor','none');
daspect([1 1 1]);
view(3);
camlight;
lighting gouraud;
box on
alpha(0.5)

%Calculate the Mathieu Parameters
Rx = interp3(XX,YY,ZZ,Vrf*phi_tot,v,0,z0*1e-6);
Ry = interp3(XX,YY,ZZ,Vrf*phi_tot,0,v,z0*1e-6);
Rz = interp3(XX,YY,ZZ,Vrf*phi_tot,0,0,z0*1e-6+v);
Fx = interp3(XX,YY,ZZ,(dc_mid+dc_end+dc_quad)/Zn/e,v,0,z0*1e-6);
Fy = interp3(XX,YY,ZZ,(dc_mid+dc_end+dc_quad)/Zn/e,0,v,z0*1e-6);
Fz = interp3(XX,YY,ZZ,(dc_mid+dc_end+dc_quad)/Zn/e,0,0,z0*1e-6+v);

%Calculate the parabolic approximation in the three primary dimensions and
%convert this into stability parameters
```

```
rx = polyfit(v(:),Rx(:),2);
ry = polyfit(v(:),Ry(:),2);
rz = polyfit(v(:),Rz(:),2);
fx = polyfit(v(:),Fx(:),2);
fy = polyfit(v(:),Fy(:),2);
fz = polyfit(v(:),Fz(:),2);
Asr = 8*Zn*e/msr/Omega^2*[fy(1) fx(1) fz(1)];
Qsr = 4*Zn*e/msr/Omega^2*[ry(1) rx(1) rz(1)];
Asrcl = 8*Zn*e/msrcl/Omega^2*[fy(1) fx(1) fz(1)];

fprintf('Asr_axial = %f \nAsr_rad1  = %f \nAsr_rad2  = %f\n',...
            Asr(1),Asr(2),Asr(3))
fprintf('Qsr_axial = %f \nQsr_rad1  = %f \nQsr_rad2  = %f\n',...
            Qsr(1),Qsr(2),Qsr(3))
fprintf('Asrcl_axial = %f \nAsrcl_rad1  = %f \nAsrcl_rad2  = %f\n',...
            Asrcl(1),Asrcl(2),Asrcl(3))
fprintf('Qsrcl_axial = %f \nQsrcl_rad1  = %f \nQsrcl_rad2  = %f\n',...
            Qsrcl(1),Qsrcl(2),Qsrcl(3))

b_sr = sqrt(Asr+Qsr.^2/2);
fsr = b_sr*Omega/2/2/pi;
fprintf('Sr Secular Frequencies (kHz):\n axial = %f\n rad1 = %f\n rad2 = %f\n',...
            fsr(1)*10^-3,fsr(2)*10^-3,fsr(3)*10^-3)
Qsrcl = 4*Zn*e/msrcl/Omega^2*[ry(1) rx(1) rz(1)];
```

Bibliography

[1] A. André, D. DeMille, J. M. Doyle, M.D. Lukin, S. E. Maxwell, P. Rabl, R. J. Schoelkopf, and P. Zoller. A coherent all-electrical interface between polar molecules and mesoscopic superconducting resonators. *Nature Physics*, 2:632–642, 2006.

[2] Paul Antohi. *Cryogenic Surface Electrode Ion Traps with Integrated Superconducting Microwave Resonators for Polar Molecular Ion Spectroscopy.* PhD thesis, Massachusetts Institute of Technology, 2011.

[3] Alexandre Blais, Ren-Shou Huang, Andreas Wallraff, S. M. Girvin, and R. J. Schoelkopf. Cavity quantum electrodynamics for superconducting electrical circuits: An architecture for quantum computation. *Phys. Rev. A*, 69(6):062320, Jun 2004.

[4] Fei Chen, A. J. Sirois, R. W. Simmonds, and A. J. Rimberg. Introduction of a dc bias into a high-q superconducting microwave cavity. *Applied Physics Letters*, 98(13):132509, 2011.

[5] J. Chiaverini, R. B. Blakestad, J. Britton, J. D. Jost, C. Langer, D. Liebfried, R. Ozeri, and D. J. Wineland. Surface-electrode architecture for ion-trap quantum information processing. *Quantum Inf. and Comp.*, 5(6):419, Sept. 2005.

[6] J. M. Chow, J. M. Gambetta, L. Tornberg, Jens Koch, Lev S. Bishop, A. A. Houck, B. R. Johnson, L. Frunzio, S. M. Girvin, and R. J. Schoelkopf. Randomized benchmarking and process tomography for gate errors in a solid-state qubit. *Phys. Rev. Lett.*, 102(9):090502, Mar 2009.

[7] L. Frunzio, A. Wallraff, D. Schuster, J. Majer, and R. Schoelkopf. Fabrication and characterization of superconducting circuit qed devices for quantum computation. *Applied Superconductivity, IEEE Transactions on*, 15(2):860 – 863, june 2005.

[8] Jiansong Gao. *The Physics of Superconducting Microwave Resonators.* PhD thesis, California Institute of Technology, 2008.

[9] Aram W. Harrow, Avinatan Hassidim, and Seth Lloyd. Quantum algorithm for linear systems of equations. *Phys. Rev. Lett.*, 103(15):150502, Oct 2009.

[10] M. G. House. Analytic model for electrostatic fields in surface-electrode ion traps. *Phys. Rev. A*, 78(3):033402, Sep 2008.

[11] D.F.V. James. Quantum dynamics of cold trapped ions with application to quantum computation. *Applied Physics B: Lasers and Optics*, 66:181–190, 1998. 10.1007/s003400050373.

[12] D. Leibfried, R. Blatt, C. Monroe, and D. Wineland. Quantum dynamics of single trapped ions. *Rev. Mod. Phys.*, 75(1):281–324, Mar 2003.

[13] David R. Leibrandt, Robert J. Clark, Jaroslaw Labaziewicz, Paul Antohi, Waseem Bakr, Kenneth R. Brown, and Isaac L. Chuang. Laser ablation loading of a surface-electrode ion trap. *Phys. Rev. A*, 76(5):055403, Nov 2007.

[14] Benjamin Mazin. *Microwave Kinetic Inductance Detectors.* PhD thesis, California Institute of Technology, 2004.

[15] Adam McCaughan. High-q superconducting coplanar waveguide resonators for integration into molecule ion traps. Master's thesis, Massachusetts Institute of Technology, 2010.

[16] T. Monz, K. Kim, A. S. Villar, P. Schindler, M. Chwalla, M. Riebe, C. F. Roos, H. Häffner, W. Hänsel, M. Hennrich, and R. Blatt. Realization of universal ion-trap quantum computation with decoherence-free qubits. *Phys. Rev. Lett.*, 103(20):200503, Nov 2009.

[17] Thomas Monz, Philipp Schindler, Julio T. Barreiro, Michael Chwalla, Daniel Nigg, William A. Coish, Maximilian Harlander, Wolfgang Hänsel, Markus Hennrich, and Rainer Blatt. 14-qubit entanglement: Creation and coherence. *Phys. Rev. Lett.*, 106(13):130506, Mar 2011.

[18] David M. Pozar. *Microwave Engineering.* John Wiley and Sons, Inc, 3rd edition, 2005.

[19] S. Seidelin, J. Chiaverini, R. Reichle, J. J. Bollinger, D. Leibfried, J. Britton, J. H. Wesenberg, R. B. Blakestad, R. J. Epstein, D. B. Hume, W. M. Itano, J. D. Jost, C. Langer, R. Ozeri, N. Shiga, and D. J. Wineland. Microfabricated surface-electrode ion trap for scalable quantum information processing. *Phys. Rev. Lett.*, 96(25):253003, Jun 2006.

[20] P. W. Shor. Algorithms for quantum computation: discrete logarithms and factoring. In *Proceedings of the 35th Annual Symposium on Foundations of Computer Science*, pages 124–134, Washington, DC, USA, 1994. IEEE Computer Society.

[21] Rainee N. Simons. *Coplanar Waveguide Circuits, Components and Systems.* John Wiley and Sons, Inc, 1st edition, 2001.

[22] A. Wallraff, D. I. Schuster, A. Blais, L. Frunzio, R. S. Huang, J. Majer, S. Kumar, S. M. Girvin, and R. J. Schoelkopf. Strong coupling of a single photon to a superconducting qubit using circuit quantum electrodynamics. *Nature*, 431:162–167, July 2004.

[23] Shannon X. Wang, Yufei Ge, Jaroslaw Labaziewicz, Eric Dauler, Karl Berggren, and Isaac L. Chuang. Superconducting microfabricated ion traps. *Applied Physics Letters*, 97(24):244102, 2010.